Volume 10
Number 6
June 2023
Pages 1521–1732

Environmental Science Nano

rsc.li/es-nano

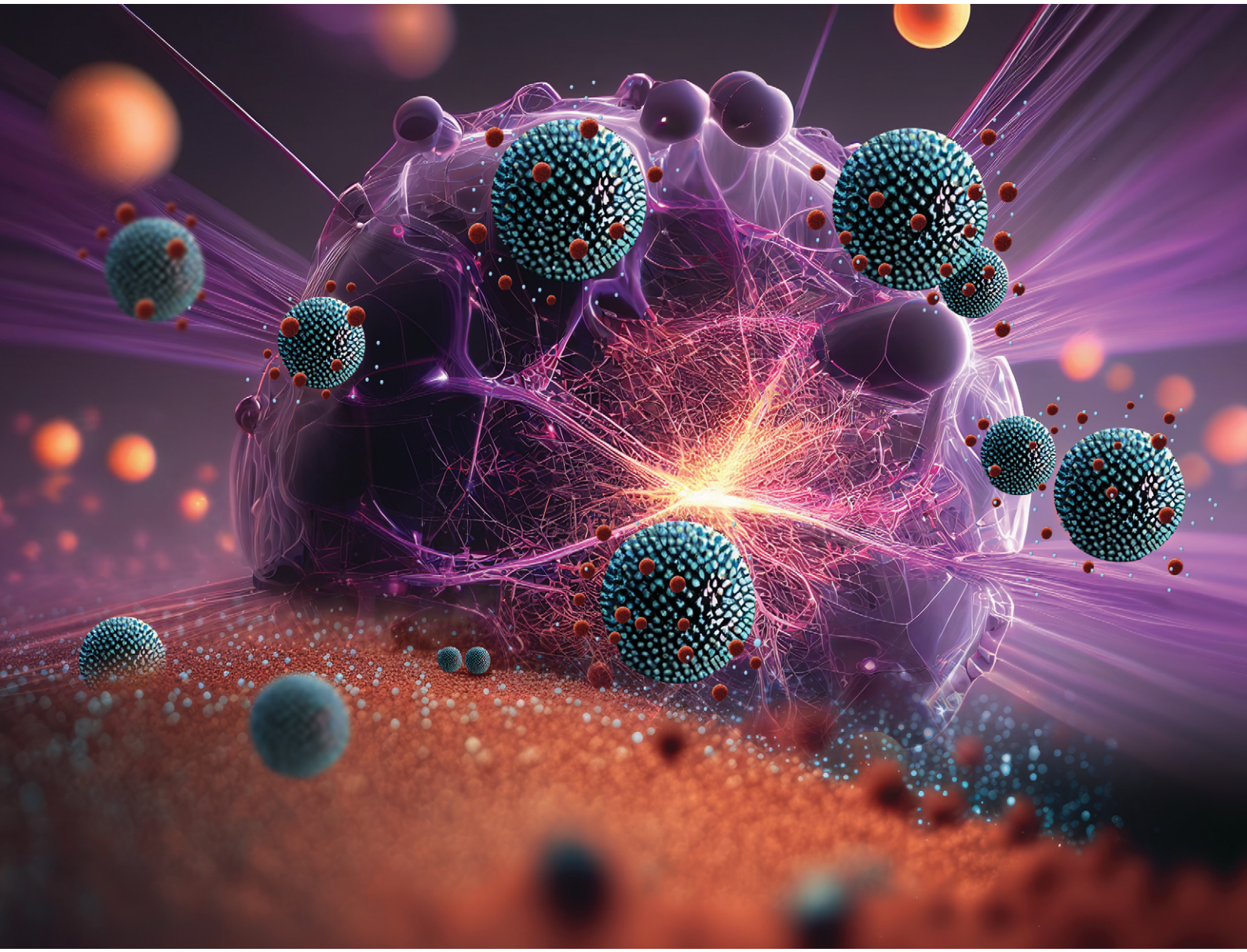

ISSN 2051-8153

ROYAL SOCIETY OF CHEMISTRY

PAPER

Swaroop Chakraborty, Peng Zhang, Superb K. Misra *et al.*
Does the doping strategy of ferrite nanoparticles create a correlation between reactivity and toxicity?

Environmental Science Nano

ROYAL SOCIETY OF CHEMISTRY

PAPER

View Article Online
View Journal | View Issue

Cite this: *Environ. Sci.: Nano*, 2023, **10**, 1553

Does the doping strategy of ferrite nanoparticles create a correlation between reactivity and toxicity?†

Swaroop Chakraborty, *[a] Dhruv Menon,[b] Venkata Sai Akhil Varri,[c] Manish Sahoo,[d] Raghavan Ranganathan,[e] Peng Zhang *[a] and Superb K. Misra *[e]

Received 6th February 2023,
Accepted 10th April 2023

DOI: 10.1039/d3en00076a

rsc.li/es-nano

Owing to their remarkable properties in terms of electrical resistivity, chemical stability, and saturation magnetisation, ferrite nanoparticles are being increasingly used for a wide range of applications. This study looks to investigate as to whether ferrite nanoparticles can be safely and viably doped with transition metal elements without adversely affecting the stability and toxicity of the nanoparticles. Monodispersed and phase pure variants of ferrites ($M_xFe_{3-x}O_4$ where M = Co, Cu, Zn, Mn) were synthesised with a size range of 9–11 nm using a wet chemistry route. The doping % within the ferrites was within the range of 15–18% for all the dopants. Compared to ferrite nanoparticles, Co and Mn doping significantly enhanced the dissolution, whereas doping with Cu and Zn had an opposite effect to dissolution. DFT calculations performed on the ferrites to calculate the vacancy formation energy of Fe and dopant atoms substantiated the experimental dissolution data. A549 cells showed a dose dependent response (10–200 μg mL^{-1}) and the reduction in cell viability followed the trend of $Mn_xFe_{3-x}O_4 > Co_xFe_{3-x}O_4 > Zn_xFe_{3-x}O_4 > Cu_xFe_{3-x}O_4 > Fe_3O_4$. A correlation study between dissolution, cell viability and uptake indicated cell viability and dissolution had a strong negative correlation for Fe_3O_4, and $Co_xFe_{3-x}O_4$ whereas for $Cu_xFe_{3-x}O_4$ this correlation was very weak. We conclude by providing an overview of the impact of doping on the safety of other metal-oxide nanoparticles (CuO, ZnO, TiO_2 and CeO_2) in comparison to ferrite nanoparticles.

Environmental significance

The strategy of doping in nanomaterials has been used to improve their physicochemical properties or to impart additional properties for use in a wide range of applications. However, there haven't been reports unravelling the impact of doping on the toxicology of nanomaterials. The overarching aim of this work is to investigate whether doping makes ferrite nanoparticles safe or unsafe. We performed a range of dissolution and ion-release studies, density functional theory studies, cellular uptake studies, cytotoxicity and reactive oxygen species generation studies to draw correlations between cell viability, cell uptake, dissolution and toxicity in an attempt to guide ferrite nanoparticle safety-by-design. The work is of profound relevance to the environmental impact of doped nanoparticles in terms of their transformations (dissolution and speciation), bio-uptake, and toxicological implications.

Introduction

Ferrites are typically obtained in one of three different crystal systems (spinel, hexagonal and garnet), and offer the means to prepare an infinite number of solid solutions, making it feasible to tailor their properties to the application at hand.[1,2] Owing to certain basic properties such as high saturation magnetization, high electrical resistivity, and superior chemical stability compared to their alternatives, ferrites have emerged as a heavily investigated class of materials over the last few decades.[1] In the biomedical domain, the possibility of preparing doped ferrite nanoparticles for their enhanced magnetic properties, for imaging and hyperthermia has expanded their applications.[2] The increased use of such customised ferrites demands a thorough investigation of their likely impact when in contact with biological and environmental entities.[3–5] In the case of humans, exposure to nanoparticles could be through inhalation, ingestion, injection and/or contact with the skin.[6,7] Owing to their small sizes, they can overcome biological barriers such as the cell membrane and can affect regular cellular processes, leading

[a] *School of Geography, Earth and Environmental Sciences, The University of Birmingham, Edgbaston, Birmingham B15 2TT, UK. E-mail: s.chakraborty@bham.ac.uk*
[b] *Cavendish Laboratory, Department of Physics, University of Cambridge, JJ Thomson Avenue, Cambridge CB3 0HE, UK*
[c] *Institute of Physics, University of Muenster, Muenster 48149, Germany*
[d] *Metallurgy Engineering and Materials Science, Indian Institute of Technology Indore, Indore, Madhya Pradesh 453552, India*
[e] *Materials Engineering, Indian Institute of Technology Gandhinagar, Palaj, Gujarat 382355, India. E-mail: smisra@iitgn.ac.in*

† Electronic supplementary information (ESI) available. See DOI: https://doi.org/10.1039/d3en00076a

to cellular dysfunction.[7–9] Scattered data on doped nanoparticle variants (CeO_2, CuO, TiO_2) have shown that dopant type and concentration does affect the cellular and ecotoxicological responses of nanoparticles.[3]

A recent study on analysis of sub-micron atmospheric particles in the UK found the overall iron content in particles <100 nm to be in the range of 10–100 ng m^{-3} and reported environmentally relevant concentrations of 50–500 μg m^{-1}.[10] Iron oxide nanoparticles are relatively less toxic at low concentrations compared to several other metal oxide nanoparticle counterparts (*viz.* CuO, ZnO). Nonetheless, they have been shown to induce toxicity due to the excessive production of reactive oxygen species (ROS) at higher concentrations.[11,12] High levels of ROS tend to damage cells through DNA damage, protein alteration, a decline in cellular physiological functioning and cell apoptosis.[12] ROS can be generated directly from the surface of some nanoparticles and contribute to oxidative stress, which impairs mitochondrial functioning and affects cellular signalling.[12,13] When observed *in vivo*, iron oxide nanoparticles undergo complicated interactions with proteins and cells, through which they get distributed to various organs, in either the particulate or metabolized form, and have shown the ability to cross the blood–brain barrier.[12,13] Following cellular uptake, these nanoparticles tend to accumulate in the endosome, where they slowly decompose into free iron, which is subsequently released into the cytoplasm.[12] Given that the ferrite nanoparticles are relatively less toxic at lower concentrations, several studies have focused on introducing transition elements (Cu, Zn, Co, Mn) as dopants to enhance certain properties. These nanoparticles are then used for applications pertaining to energy, gas-sensing, thin films and catalysis.[14–17] Despite these advances, the impact of doping on the safety-by-design of ferrite nanoparticles has not been studied extensively, and given the large-scale industrial use of these nanoparticles, such a study becomes essential. In fact, the current data and overall understanding of metal-oxide nanomaterial release from nanomaterial-containing products is largely incomplete,[18] with no systematic study comparing the relative impact and application ratios of these materials, to guide safety-by-design. We thus feel that there is a pressing need for a systematic study that correlates and compares the impact of various metal-oxide nanoparticles, and have attempted to do so for doped ferrite nanoparticles.

To probe the impact of dopants, $Cu_xFe_{3-x}O_4$, $Co_xFe_{3-x}O_4$, $Mn_xFe_{3-x}O_4$, and $Zn_xFe_{3-x}O_4$, nanoparticles were subjected to toxicological profiling in a lung epithelial cell line (A549). These studies were complemented with dissolution and ion-release studies, cellular uptake studies, and cytotoxicity and ROS generation studies. The ion-release studies were supported by density functional theory (DFT) calculations of the vacancy formation energies as a proxy for the dissolution potential of each ferrite nanoparticle. The overarching aim of this study is to demonstrate the impact of transition element (Cu, Zn, Co, Mn) doping on the toxicity of ferrite nanoparticles. We present a correlation between cell viability-cellular uptake-dissolution for all the doped ferrite variants. The scope of this study is also to understand the extent of toxicity generated due to dissolved ions *versus* the particulates affecting the safety by design of ferrite nanoparticles.

Materials and methods

Materials

All the chemicals and reagents used in conducting the experiments were purchased from Merck-Sigma-Aldrich and were of analytical grade. The separation of particles from the dissolved species was performed using Amicon Ultrafiltration Tubes (MWCO: 3 kDa) purchased from Merck, India. A-549 lung carcinoma cells (*Homo sapiens*) were procured from ATCC. Dulbecco's modified Eagles medium (DMEM), fetal bovine serum (FBS), 3-(4,5dimethylthiazol-2-yl)-2,5-diphenyltetrazolium bromide (MTT) dye, and 2,7-dichlorofluorescein diacetate (DCFDA) were purchased from Himedia Limited, India. The Fe, Cu, Zn, Mn, and Co standards for ICP-MS analysis were purchased from Perkin Elmer, USA., USA.

Synthesis of ferrite nanoparticles ($M_xFe_{3-x}O_4$, where M = Co, Cu, Zn and Mn)

Ferrite nanoparticles were synthesized using a co-precipitation method followed by microwave irradiation. Briefly, 3.2 M of sodium hydroxide solution was prepared at a volume of 20 mL and challenged with 40 mL of 2 mM $FeCl_3{\cdot}6H_2O$ and 1 mM $FeCl_2{\cdot}4H_2O$. The resulting precipitate suspension was stirred for 30 minutes and transferred to a 100 mL ceramic crucible. Later, the precipitates were subjected to microwave irradiation (100 °C and 30 bar pressure) to obtain undoped Fe_3O_4 nanoparticles. Subsequently, they were cooled to room temperature naturally. After repeated washing with ultrapure water and ethanol, the nanoparticles were centrifuged at 8000 rpm (8229 × *g*) for 10 min and the pellet was dried in an oven. After drying overnight, the pellet was stored for further experiments.

Similar protocols were followed for the synthesis of Cu, Co, Zn and Mn-doped ferrite nanoparticles ($Cu_xFe_{3-x}O_4$, $Co_xFe_{3-x}O_4$, $Zn_xFe_{3-x}O_4$ and $Mn_xFe_{3-x}O_4$.). Briefly, the respective salts of the dopants ($MnCl_2{\cdot}4H_2O$; $CuCl_2{\cdot}2H_2O$; $ZnCl_2{\cdot}2H_2O$; $COCl_2{\cdot}6H_2O$) were weighed equal to 20% of the Fe salts used for undoped nanoparticle synthesis. NaOH solution with a concentration of 3.2 M was prepared at a volume of 20 mL and mixed with 40 mL of 0.6 mM of X (Cu, Mn, Co, Zn) salts, 1.6 mM $FeCl_3{\cdot}6H_2O$ and 0.8 mM $FeCl_2{\cdot}4H_2O$. The molar concentrations of the all the precursors used is shown in Table S1.† The precipitate suspension was transferred to a 100 mL ceramic crucible. Later, the precipitates were subjected to microwave irradiation (100 °C and 30 bar pressure) to obtain doped ferrite nanoparticles. These nanoparticles were washed several times (8229 × *g*) with ultrapure water and ethanol until the pH of the solution turned neutral (washing of unreacted precursors) and dried in an oven overnight at 50 °C.

Physicochemical characterization

The synthesized doped and undoped ferrite nanoparticles were subjected to a wide range of analytical techniques to investigate their physicochemical properties. Identification of the compound and its phase purity were assessed through powder X-ray diffractometer (PXRD, Bruker D8, Cu-Kα, 40 kV, 30 mA, 2θ = 20–80°). The diffraction patterns obtained from Fe_3O_4, $Cu_xFe_{3-x}O_4$, $Co_xFe_{3-x}O_4$, $Zn_xFe_{3-x}O_4$, $Mn_xFe_{3-x}O_4$ were compared with that of the Inorganic Crystal Structure Database (ICSD) to deduce their phase purity. The morphology and size distribution of the nanoparticles was investigated using Transmission Electron Microscopy (Themis, FEI, 200 kV). Size distribution analysis was performed on TEM images using ImageJ software. Inductively Coupled Plasma-Mass Spectrometry analyses (ICP-MS, Nexion 2000, Perkin Elmer, USA) were performed to quantify the concentration of each dopant in the ferrite nanoparticles. Appropriate amounts of doped and undoped samples were digested in an *aqua regia* acid mixture using an open digestion method (120 °C, 20 min) until the samples turned clear. The digested samples were cooled down at room temperature, filtered and diluted with 2% ultrapure nitric acid (70% Nitric Acid, Suprapure, Merck) for ICP-MS analysis. The surface composition and elemental valence states of Fe_3O_4, $Cu_xFe_{3-x}O_4$, $Co_xFe_{3-x}O_4$, $Zn_xFe_{3-x}O_4$, $Mn_xFe_{3-x}O_4$ were investigated using X-ray photoelectron spectroscopy (Thermo Scientific, NEXSA XPS, Al Kα, 1486 eV and 72 W). The high-resolution spectra of C-1s, O-1s, Fe-2p, Cu-2p, Mn-2p, Zn-2p and Co-2p were measured at the constant analyzer energy (CAE) with a step size and pass energy of 0.1 eV and 50 eV, respectively. The data acquisition took place with a step size and dwell time of 0.1 eV and 700 s. The binding energies for all of the samples were corrected with carbon references at 284.6 eV. The sedimentation behaviour and hydrodynamic size of the ferrite variants were measured in cell culture media (DMEM with 10% FBS) using Malvern Nano ZS (Malvern Panalytical, UK) for 72 h to remain consistent with other time-dependent experiments (*e.g.*, dissolution, uptake, and cytotoxicity studies). The surface charge and isoelectric point of various ferrite samples were evaluated using zeta potential measurements.

Batch dissolution study

To investigate the dissolution of ferrite variants, they were subjected to time-dependent dissolution experiments (n = 3) for up to 72 h in complete cell culture media (CCM, DMEM with 10% FBS, pH ~7.4). Briefly, 100 μg mL^{-1} of Fe_3O_4, $Cu_xFe_{3-x}O_4$, $Co_xFe_{3-x}O_4$, $Zn_xFe_{3-x}O_4$, $Mn_xFe_{3-x}O_4$ nanoparticles were suspended separately in 100 mL of CCM in a wide mouth plastic bottle and incubated at 37 °C, 150 rpm in a shaking incubator. At several time points, 1 mL of sample was withdrawn from each bottle containing the nanoparticle suspensions and they were subjected to centrifugal ultrafiltration using ultrafiltration tubes (MWCO: 3 kDa) at 6000 rpm (4629 × g) for 10 min. The filtrates were collected from the bottom of the tubes and were acidified using 2% nitric acid for the ICP-MS analysis. The ICP-MS analysis was performed to detect Fe, Cu, Co, Mn, and Zn in helium KED mode.

Intracellular trafficking of ferrite nanoparticles

The trafficking of Fe_3O_4, $Cu_xFe_{3-x}O_4$, $Co_xFe_{3-x}O_4$, $Zn_xFe_{3-x}O_4$, and $Mn_xFe_{3-x}O_4$ nanoparticles were measured in lung adenocarcinoma cells to investigate the trend of nanoparticle uptake across the undoped and doped ferrite nanoparticles. In this experiment, 100 μg mL^{-1} of each ferrite nanoparticle was exposed to 2.0 × 10^5 cells for 24 h, 48 h and 72 h in a 6-well plate. PBS was used as a negative control exposure to the cells. After each incubation time point (24 h, 48 h, 72 h), the cells were thoroughly washed with 1× PBS to remove excess nanoparticles that might alter the uptake results. Later, the cells were harvested by trypsinisation and were collected in a separate tube. The harvested cells were freeze-dried and digested using an ashing mixture (3 : 1 molar ratio of HNO_3 and H_2O_2) under heating conditions. The digested samples were acidified using 2% nitric acid and the total uptake was measured using ICP-MS. The calibration curve was made to detect Fe, Cu, Co, Mn, and Zn in a range of 0.0001 to 1 μg mL^{-1} using the ionic standard of the respective elements. The measurement was carried out in helium KED mode (dwell time = 50 ms, sweeps/readings 50, helium gas flow 3.5 mL min^{-1}, Syngistix software). The net uptake was calculated using eqn (1).

$$\text{Total uptake} = \frac{C(\text{Fe}) + C(\text{X})}{C(\text{cells})} \quad (1)$$

where, C(Fe) is the measured concentration of Fe in the samples (μg mL^{-1}), C(X) is the measured concentration of the dopant (Cu, Mn, Co, Zn) (μg mL^{-1}) and C(Cells) is the concentration of cells (cells mL^{-1}) in the samples.

Cytotoxicity and oxidative stress analysis

An MTT assay (n = 3) was performed to investigate the toxicity of undoped and doped ferrite nanoparticles. Briefly, 96 well plates were seeded with 5 × 10^3 cells/well and were exposed to nanoparticles at a concentration of 10–200 μg mL^{-1} for a period of 72 h. 2% H_2O_2 was used as a positive control whereas, 1× PBS was used as a negative control. The time-dependent cytotoxicity was measured for 24 h, 48 h, and 72 h at 590 nm using a multimode plate reader (Biotek, Synergy HT spectrophotometer). The cell viability was calculated using eqn (2).

$$\text{Cell viability} = \frac{A(\text{s}) - A(\text{m})}{A(\text{c}) - A(\text{m})} \quad (2)$$

where: A(s) is the absorbance of the samples in presence of nanoparticles, A(m) is the absorbance of a blank CCM, and A(c) is the absorbance of the CCM with cells and no nanoparticles.

Oxidative stress in the cells was investigated by measuring the reactive oxygen species using DCFDA assay. Briefly, black opaque 96 well plates were seeded with 5 × 10^3 cells/well and

exposed to nanoparticles at a concentration of 10–200 μg mL^{-1} for a period of 72 h (n = 3). Post-exposure, the cells were thoroughly washed with 1× PBS to remove the nanoparticles in the samples. The cells were exposed to 200 μL of 20 μM DCF-DA and incubated at 37 °C for 30 min. After incubation, the cells were washed with 1× PBS to remove the unreacted dye and the fluorescent intensity was measured using a multimode plate reader (Biotek, Synergy HT spectrophotometer). The fold changes in ROS production were calculated with respect to control.

Ion *versus* particulate mediated cell uptake and viability

To investigate the intracellular uptake and cytotoxicity caused by undoped and doped ferrite nanoparticles and their dissolved species, a series of cellular uptake and cytotoxicity studies were performed. In this experimental setup, two distinct scenarios were considered in terms of ionic exposure, 1) if the ferrite nanoparticles undergo complete dissolution (*i.e.*, 100% nanoparticles dissolve in CCM), and 2) the realistic ionic release as calculated in the batch dissolution experiment. Stock solutions for Fe ions, Cu ions, Co ions, Mn ions and Zn ions were prepared using their respective chloride salts. In ionic uptake studies, an equivalent concentration of 100 μg mL^{-1} (considering 100% dissolution of undoped and doped ferrite variants) of Fe ions, Cu ions, Co ions, Mn ions and Zn ions were exposed to 2.0×10^5 cells for 24 h, 48 h and 72 h in a 6 well plate. The objective of performing this experiment is to investigate the extent of toxicity that both doped and undoped ferrites could cause if they undergo complete dissolution. For clarity, we have represented the exposure ionic concentrations in both the scenarios, for doped and undoped ferrite variants.

2.0×10^5 cells were exposed to equivalent ionic concentrations (as calculated from dissolution experiments) of Fe, Cu, Co, Mn and Zn for 24 h, 48 h and 72 h in a 6-well plate. After each incubation time point, the cells were thoroughly washed using 1× PBS, harvested by trypsinisation and collected in a separate tube. The harvested cells were freeze-dried and digested using an ashing mixture (3 : 1 molar ratio of HNO_3 and H_2O_2) under heating conditions. The digested samples were acidified using 2% nitric acid and the total uptake was measured using ICP-MS. Similarly, cell viability assays were performed using both scenarios mentioned previously. The equivalent concentration as that of undoped and doped ferrites undergoing complete dissolution and realistic dissolution values were exposed to 5×10^3 cells/well. The cell viability data obtained from the ionic studies were correlated with the cell viability data obtained from nanoparticle exposure. All the experiments were performed in triplicate (n = 3) to investigate the statistical significance of the data.

Computational details

DFT-based first-principles calculations for vacancy formation energy for all the systems *i.e.*, ferrite and other spinel ferrite systems (MFe_2O_4 where M = Co, Cu, Zn and Mn) were performed on Vienna *Ab initio* Simulation Package (VASP)[19] version 6.3.0. All calculations utilise a plane wave basis set for expansion of electron wavefunctions[20] and further use Projector Augmented Wave (PAW)[21] pseudopotentials for approximating the exchange–correlation functional, which for the systems under consideration are obtained from the Perdew–Burke–Ernzerhof (PBE) generalised gradient approximation (GGA) scheme.[22] The vacancy formation energy was calculated for each system using eqn (3).[23]

$$E_{VF} = (E_V + E_{M/Fe}) - E_o \quad (3)$$

Here, E_{VF} represents the vacancy formation energy for the system; E_o represents the ground state energy of the defect-free supercells and, E_V refers to the ground state energy of the supercell with one random vacancy introduced by the removal of either a substituent (M) atom in the case of doped ferrite or a Fe atom in the case of undoped ferrite. $E_{M/Fe}$ is the energy of a single Fe/M atom that has been removed to create a vacancy in its most stable state and was calculated as the energy per atom of a defect-free unit cell of the particular element in its equilibrium crystal structure at 0 K (Fig. 1). All the aforementioned energies were obtained by performing self-consistent field (SCF) calculations while considering the ions in the supercell to be fixed in their experimentally reported lattice positions. Ionic relaxations were avoided to be able to accurately model only a single vacancy formation energy in an infinite lattice, for which the ionic cores must be essentially unperturbed.[24] Two different vacancy formation energies had to be calculated for all the systems either pertaining to the different element types (M and Fe vacancies for spinel ferrites) or the same element type being present in sites with different coordination numbers within the supercell (Fe in Fe_3O_4 in octahedral and tetrahedral sites). More details related to the computational experimentation is added in ESI† (section S1).

Statistical analysis

Dissolution studies, cellular uptake studies and cell cytotoxicity assays were performed in triplicate (n = 3). All data were represented as mean ± standard deviation. For all biological experiments, analysis of variance (ANOVA) was performed to identify the p values as compared to the control. The differences were statistically significant at values of $*p < 0.05$, $**p < 0.01$, and $***p < 0.001$. A correlational analysis between the dissolution, cell uptake and cytotoxicity was performed using Pearson's correlation coefficient in Origin Labs software version 9.2.

Results and discussion

Characterization of ferrite nanoparticles

The ultrafine nanoparticles obtained through co-precipitation under reflux were characterized using an array of physicochemical characterization techniques. TEM images revealed that Fe_3O_4 (Fig. 2a), $Cu_xFe_{3-x}O_4$ (Fig. 2b), $Co_xFe_{3-x}O_4$ (Fig. 2c), $Zn_xFe_{3-x}O_4$ (Fig. 2d) and $Mn_xFe_{3-x}O_4$ (Fig. 2e) have

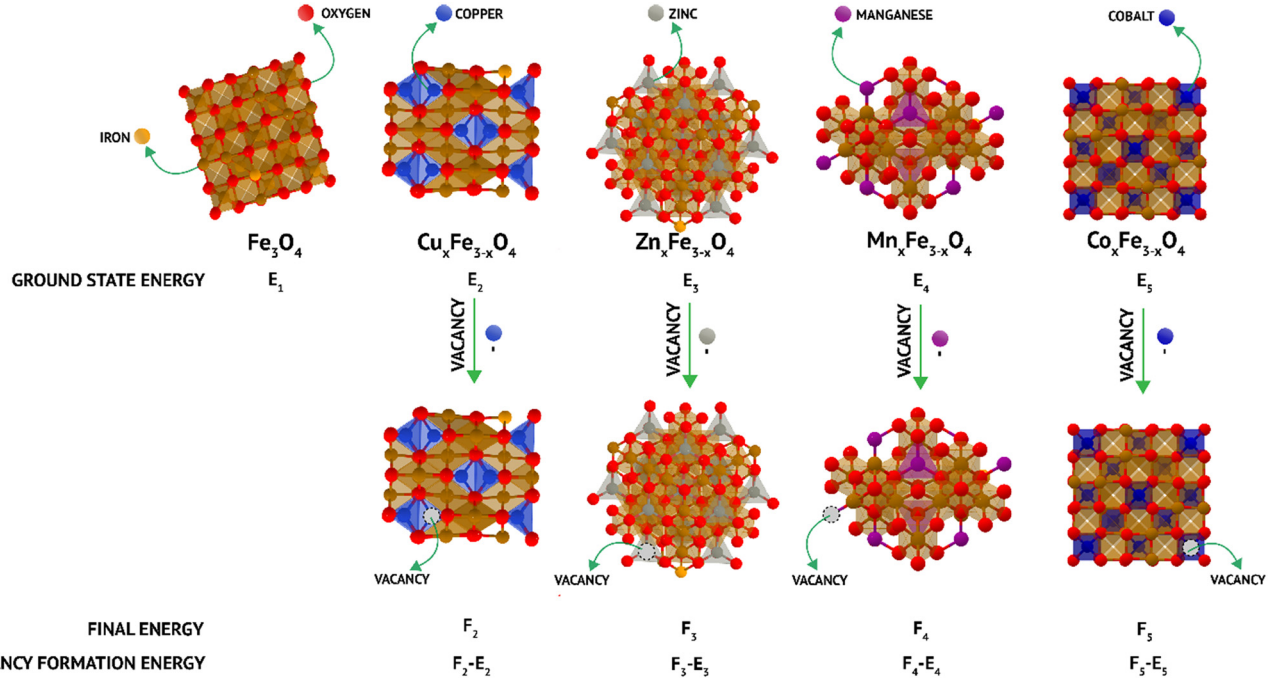

Fig. 1 Schematic of density functional theory (DFT) calculations of the vacancy formation energy in doped and undoped ferrites.

similar morphologies and an average particle size of 11.5 ± 3.5 nm for Fe_3O_4 nanoparticles, 9.9 ± 3.2 nm for $Cu_xFe_{3-x}O_4$ nanoparticles, 11 ± 2.9 nm for $Co_xFe_{3-x}O_4$ nanoparticles, 10.2 ± 3.7 nm for $Zn_xFe_{3-x}O_4$ nanoparticles and 8.6 ± 2.7 nm for $Mn_xFe_{3-x}O_4$ nanoparticles. The size reduction was statistically significant for $Mn_xFe_{3-x}O_4$ ($^{**}p < 0.01$) nanoparticles, whereas for $Cu_xFe_{3-x}O_4$ ($p < 0.1$), $Zn_xFe_{3-x}O_4$ ($p < 0.2$), and $Co_xFe_{3-x}O_4$ ($p < 0.6$) nanoparticles the size difference was

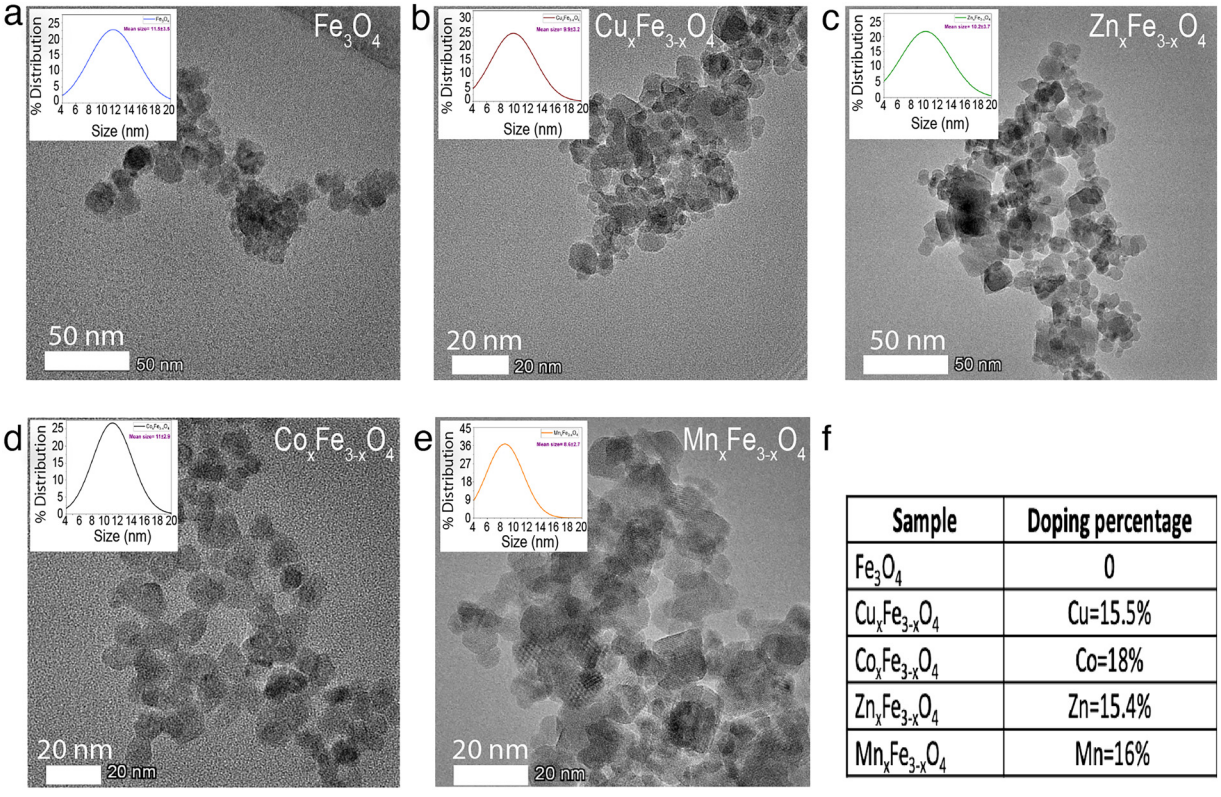

Sample	Doping percentage
Fe_3O_4	0
$Cu_xFe_{3-x}O_4$	Cu=15.5%
$Co_xFe_{3-x}O_4$	Co=18%
$Zn_xFe_{3-x}O_4$	Zn=15.4%
$Mn_xFe_{3-x}O_4$	Mn=16%

Fig. 2 TEM images showing the morphology and particle size distribution (shown in inset) of (a) Fe_3O_4 (b) $Cu_xFe_{3-x}O_4$ (c) $Co_xFe_{3-x}O_4$ (d) $Zn_xFe_{3-x}O_4$ (e) $Mn_xFe_{3-x}O_4$, (f) dopant concentration in ferrites as measured by ICP-MS.

not significant. From the ICP-MS measurement data, the doping percentages of the transition metals is represented in Fig. 2f. Owing to incompatible surface energies, Cu is much more likely to occupy interstitial sites in the Fe_3O_4 matrix than to be loosely bound to the surface. This observation is supported by similar atomic radii of Cu and Fe, which makes it easier for Cu to occupy interstitial sites in the matrix. In comparison, Zn, Co, and Mn have larger atomic radii than Fe, as a result of which, if these atoms were to occupy interstitial sites in the matrix, a large strain would be generated. This hypothesis is supported by the large peak shifts in the XRD measurements (Fig. 2a). Based on the stoichiometric calculations as per the ICP-MS measurement, the composition of doped ferrites was $Cu_xFe_{3-x}O_4$ ($Cu_{0.89}Fe_{2.1}O_4$), $Co_xFe_{3-x}O_4$ ($Co_{1.45}Fe_{1.54}O_4$), $Zn_xFe_{3-x}O_4$ ($Zn_{1.26}Fe_{1.73}O_4$) and $Mn_xFe_{3-x}O_4$ ($Mn_{1.5}Fe_{1.5}O_4$).

XRD measurements were carried out to identify the crystalline structure of the elements. In the case of Fe_3O_4 nanoparticles, six characteristic peaks at 2θ values of 30°, 35°, 43°, 55°, 57° and 62° corresponding to the (220), (311), (400), (422), (511) and (440) planes were observed (Fig. 3a). XRD measurements did not reveal any new peaks (Fig. 3a) for the doped ferrite nanoparticles, which demonstrates the phase purity of the synthesized nanoparticles. Upon the introduction of the dopant ions into the system, in each case, a peak shift was observed in the XRD patterns attributed to a decrease in one of the lattice dimensions. This decrease has been attributed to some of the Fe–O bonds in Fe_3O_4 being substituted by M–O bonds (M = Cu, Zn, Co or Mn).[25] This observation is supported by the shifting of peaks in the case of the doped variants indicating an increased loading of the crystal. Additionally, the broadening of the peaks was observed for the doped variants due to the loss in ordering due to the occupation of the interstitial sites (Fig. 3a). XPS measurements on Fe_3O_4 nanoparticles showed a characteristic peak at 709.5 eV assigned to Fe $2p_{3/2}$.[26,27]

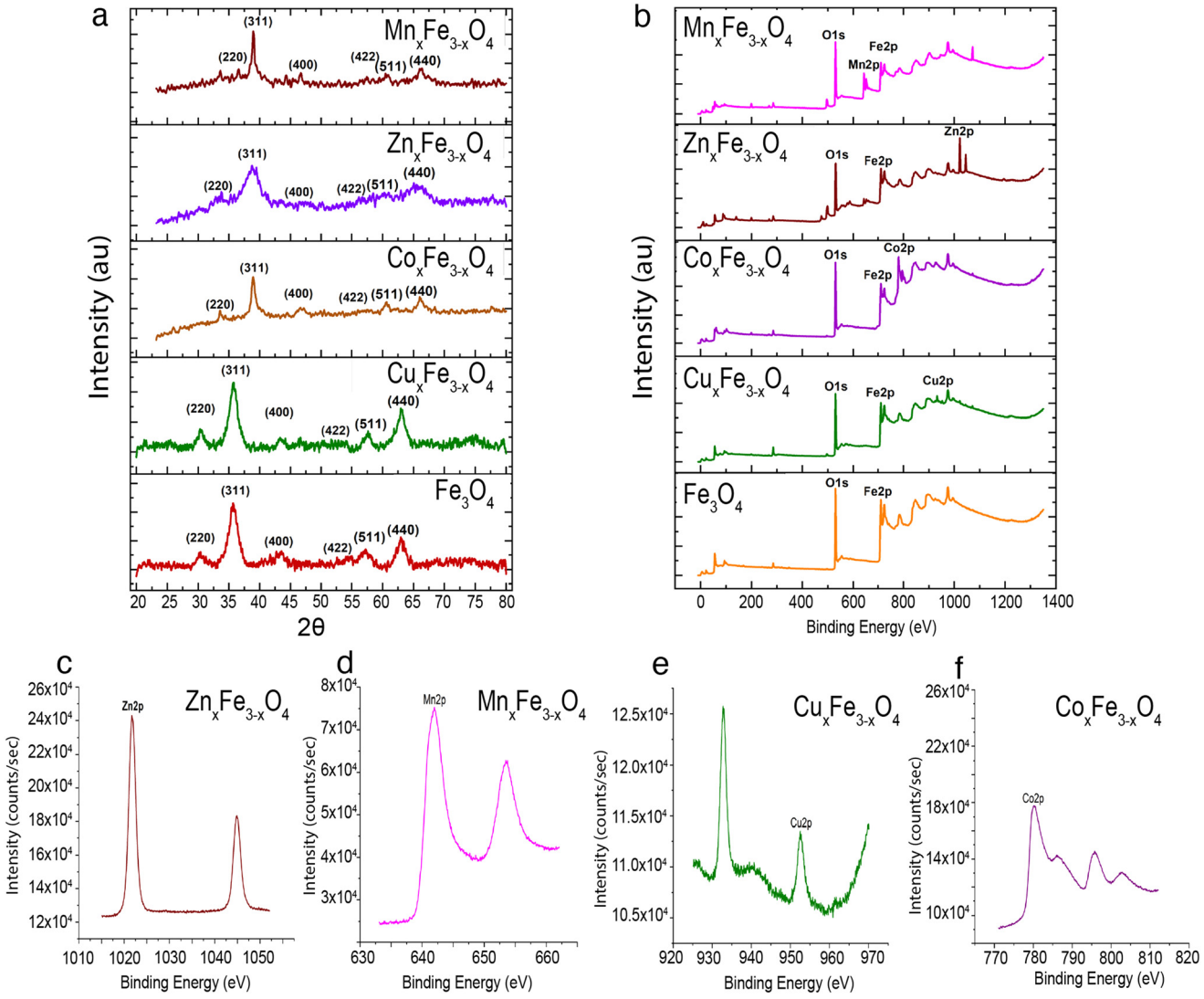

Fig. 3 Chemical characterization of various doped ferrite nanoparticles (a) XRD spectral pattern of the ferrite variants. (b) XPS spectral pattern of the ferrite variants. (c–f) Magnified XPS spectrum of individual dopants present in the ferrites to demonstrate their characteristics peaks.

Characteristic peaks at 528.5 eV, 529.7 eV and 530.7 eV corresponding to O 1s were observed.[26] In the case of $Cu_xFe_{3-x}O_4$, additional peaks were resolved at 932.5 eV and 952.5 eV corresponding to Cu $2p_{3/2}$ and Cu $2p_{1/2}$, respectively (Fig. 3b and e). For $Co_xFe_{3-x}O_4$, the additional peak at 781.5 eV and the satellite peak at 786.5 eV is ascribed to Co $2p_{3/2}$, while the peak at 796.5 eV is ascribed to Co $2p_{1/2}$ (Fig. 3b and f).[28] For $Zn_xFe_{3-x}O_4$, Zn $2p_{3/2}$ was deconvoluted into two peaks at binding energies of 1022 eV and 1045 eV (Fig. 3b and c).[29] Lastly, in the case of $Mn_xFe_{3-x}O_4$, Mn 2p has broad peaks at 642 eV (Mn $2p_{3/2}$) and 652 eV (Mn $2p_{1/2}$) (Fig. 3b and d). The characteristic peaks of respective dopants in the XPS spectra confirm the presence of the doping elements within the ferrite nanoparticles.

Suspension characteristics of ferrite nanoparticles

The zeta potential values at pH 7 for each variant of ferrite nanoparticles were measured to be Fe_3O_4 (+7.07 mV), $Cu_xFe_{3-x}O_4$ (−23.55 mV), $Co_xFe_{3-x}O_4$ (+17.22 mV), $Zn_xFe_{3-x}O_4$ (−4.47 mV) and $Mn_xFe_{3-x}O_4$ (−20.09 mV). The net surface charge at neutral pH for each ferrite variant is different. In the case of Fe_3O_4 and $Co_xFe_{3-x}O_4$, the surface zeta potential was observed to be positive, whereas the other three variants (*i.e.*, $Cu_xFe_{3-x}O_4$, $Zn_xFe_{3-x}O_4$, $Mn_xFe_{3-x}O_4$) showed a net negative charge at the neutral pH. Zeta potential measurements were carried out on all variants of ferrites to determine their isoelectric points (IEP). These measurements revealed that the IEP of Fe_3O_4 nanoparticles in ultrapure water was 7.8 (Fig. 4b), which is consistent with values reported in the literature.[30,31] At near neutral pH, the zeta potentials ranged from −24 ± 0.15 mV to 21 ± 0.41 mV, with Fe_3O_4 and $Zn_xFe_{3-x}O_4$ having the least suspension stability, implying that they were most likely to agglomerate. These observations are confirmed by hydrodynamic size measurements which revealed that $Co_xFe_{3-x}O_4$ and $Mn_xFe_{3-x}O_4$ have relatively higher suspension stability in complete media (DMEM with 10% FBS) (Fig. S4a†). Compared to these two variants, the others seem to undergo sedimentation, which is highest in the case of Fe_3O_4. After 24 h of exposure, the hydrodynamic size of Fe_3O_4 drastically reduced (29.8%) from 338 ± 13 nm to 237 ± 18 nm, which after 72 h of exposure further reduced to 189 ± 5 nm (44%). This corresponds to a high rate of sedimentation of particles owing to poor stability in the cell culture media. In the case of $Cu_xFe_{3-x}O_4$ and $Zn_xFe_{3-x}O_4$, the hydrodynamic stability was drastically affected by the degree of nanoparticle sedimentation with time. For instance, the hydrodynamic size of $Cu_xFe_{3-x}O_4$ was 292 ± 20 nm at 0 h, which was reduced by 16% in 24 h (241 ± 13 nm) and

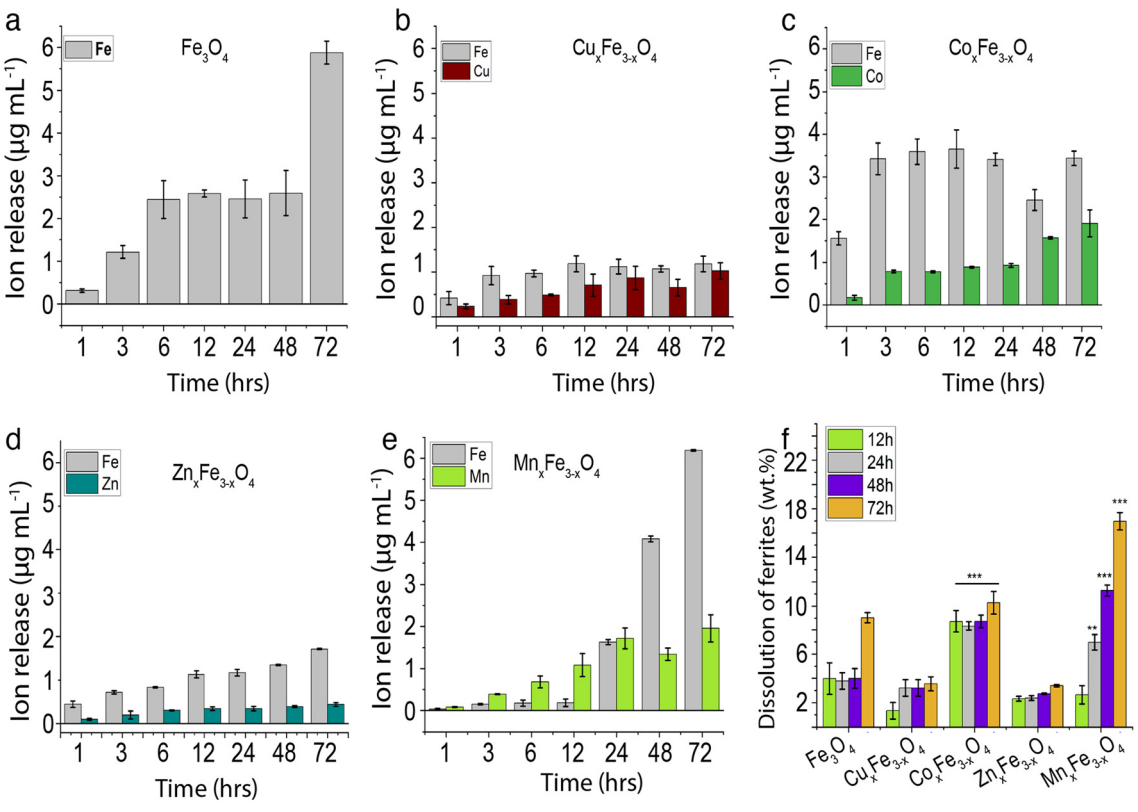

Fig. 4 Experimental results of ion release during dissolution studies on ferrite variants. (a) Ionic release profile for Fe_3O_4 (b) ionic release profile for $Cu_xFe_{3-x}O_4$. (c) Ionic release profile for $Co_xFe_{3-x}O_4$. (d) Ionic release profile for $Zn_xFe_{3-x}O_4$. (e) Ionic release profile for $Mn_xFe_{3-x}O_4$. (f) Profile of the % dissolution (wt%) of ferrites with time. The concentration of each ferrite variant used for the experiments was 100 μg mL^{-1} up to 72 h in complete media (DMEM, 10% FBS). The experiments were performed in triplicate (n = 3). The statistical significance was calculated with respect to the dissolution values of Fe_3O_4.

further reduced by 56% (128 ± 5 nm) in 72 h. Similar observations were made in the case of $Zn_xFe_{3-x}O_4$, wherein the nanoparticle sizes were reduced by 40% (259 ± 6 nm at 0 h to 148 ± 11 nm at 72 h). In comparison, after 24 h hydrodynamic size of $Co_xFe_{3-x}O_4$ nanoparticles reduced only by 18.2% (246 ± 10 nm to 201 ± 9 nm) in 24 h and remains stable thereafter, whereas for $Mn_xFe_{3-x}O_4$ the reduction was 10% (222 ± 10 nm to 198 ± 4 nm) after 24 h and were suspension stable until 72 h. The values of hydrodynamic stability of these ferrite nanoparticles are largely dependent on their sedimentation rate and have a clear role in their dissolution. It is because the colloidal stability of the particles governs the particle-media interactions and hence, enhances or reduces the amount of dissolution.

Dissolution behaviour of ferrite nanoparticles

Dissolution profiles for the ferrite variants are plotted for Fe and the respective dopants. These observations are important because in most cases, it is the dopant ions that are more toxic. Moreover, these observations would give key insights into the type of interactions between the dopant ions and Fe in the matrix. For Fe_3O_4 nanoparticles over a period of 48 h in cell culture medium 2.6 μg mL^{-1} of Fe was observed to leach out from the nanoparticles, and this increased to 5.9 μg mL^{-1} in 72 h (Fig. 4a). By introducing 15.5% of Cu into ferrite nanoparticles ($Cu_xFe_{3-x}O_4$), we observed a decrease in the release of Fe into the cell culture medium. The maximum release of Fe was recorded to be 1.2 μg mL^{-1} over the 72 h period. Although for the initial time point, Cu release was less compared to Fe, at the end of 72 h there was no significant difference observed. This observation is supported by a couple of pieces of evidence. Firstly, the hydrodynamic stability was drastically reduced with time (Fig. S4a†), coupled with a high sedimentation rate and a high amount of agglomerated nanoparticles. This reduces the overall particle-media interactions, consequently, reducing the dissolution. Secondly, as shown in DFT studies (Table 2), there is a strong interaction between Cu and Fe in the matrix, leading to a controlled release of these ions in cell culture media. However, for $Co_xFe_{3-x}O_4$ there was no suppression in the release of Fe, rather a marginal increase in the Fe release over the 72 h period. Co release from $Co_xFe_{3-x}O_4$ nanoparticles also increased with immersion time in cell culture medium, with up to 3.43 ± 0.16 μg mL^{-1} and 1.91 ± 0.03 μg mL^{-1} Fe and Co release after 72 h. Similarly, $Mn_xFe_{3-x}O_4$ showed Fe release to be 6.1 ± 0.01 μg mL^{-1} and Mn release to be 1.95 ± 0.3 μg mL^{-1} after 72 h of exposure. The concentration of Fe rapidly rose to 6.18 ± 0.017 μg mL^{-1} and for Mn, it increased to 1.95 ± 0.32 μg mL^{-1} at the end of 72 h of exposure. This highlights weak interactions between Fe and Mn, leading to a much higher release of ions in the media as demonstrated by the vacancy formation energy and binding energy data in DFT studies (Table 2).

The ion release profiles (Fig. 4b–e) show the consequence of introducing a second metal ion. The lowest release of Fe ions was seen in the case of $Cu_xFe_{3-x}O_4$ (Fig. 4b), while $Mn_xFe_{3-x}O_4$ showed a high release of Fe after 72 h (Fig. 4e). Dissolution profiles in terms of wt% are shown in Fig. 4f, wherein the cumulative release of all ions (Fe and dopant) is considered in measuring the overall wt% dissolution. For Fe_3O_4 nanoparticles there was a 4% dissolution over 48 h, which increased to 9% after 72 h (Fig. 4e). The dissolution was the lowest for $Cu_xFe_{3-x}O_4$, which showed ~1% dissolution after 12 h, with an increased to 3% at 72 h (Fig. 4b). On the other hand, % dissolution was much higher in the case of $Co_xFe_{3-x}O_4$ as compared to the other variants with 9% after 12 h, gradually increasing to 11% by 72 h (Fig. 4c). $Zn_xFe_{3-x}O_4$ showed an overall % dissolution very similar to $Cu_xFe_{3-x}O_4$, with 2% in the first 12 h, gradually increasing to 3% by the 72 h (Fig. 4d). A linear increase was observed in the case of $Mn_xFe_{3-x}O_4$ with 3% dissolution after the first 12 h and increasing to 17% at 72 h (Fig. 4e). Higher dissolution was observed in the case of $Mn_xFe_{3-x}O_4$ and $Co_xFe_{3-x}O_4$ (Fig. 4f), which also showed better suspension stability in CCM (Fig. S4a†). However, in the case of Fe_3O_4, $Cu_xFe_{3-x}O_4$ and $Zn_xFe_{3-x}O_4$, lower hydrodynamic stability with respect to time with a higher sedimentation rate didn't allow them to have prolonged interaction with the media owing to low dissolution. Additionally, the change in the lattice geometry on the introduction of the dopant into Fe_3O_4 and the dopant–oxygen bond energies would also influence their interactions with the media. Due to the complexity of the factors involved, it becomes difficult to gauge their exact roles in nanoparticle dissolution.[32]

The trends observed experimentally are reflected in vacancy formation energy calculations carried out on the undoped and doped ferrite variants in their bulk forms (Fig. 1 and Table 2). In the case of Fe leaching out of the matrix, the calculations point towards a decrease in Fe

Table 1 Physicochemical properties of doped and undoped ferrite nanoparticles

Parameters	Fe_3O_4	$Cu_xFe_{3-x}O_4$	$Co_xFe_{3-x}O_4$	$Zn_xFe_{3-x}O_4$	$Mn_xFe_{3-x}O_4$
Composition		$Cu_{0.89}Fe_{2.1}O_4$	$Co_{1.45}Fe_{1.54}O_4$	$Zn_{1.26}Fe_{1.73}O_4$	$Mn_{1.5}Fe_{1.5}O_4$
[a]Size (nm)	11.5 ± 3.5	9.9 ± 3.2	11 ± 2.9	10.2 ± 3.7	8.6 ± 2.7
Crystallite size (nm)	5.01	5.41	3.7	3.03	8.5
Zeta potential (mV) (pH 7.0)	+7.07	−23.55	+17.22	−4.47	−20.09
Fe concentration (μg mL^{-1})	65.6	52.17	38	36.6	32
Dopant concentration (μg mL^{-1})		15.8	18.4	15.4	16

[a] Size measured using TEM; n = 100 and data is presented as mean ± std.dev.

Table 2 Vacancy formation energy calculated using DFT

Ferrites	E_O (eV)	E_V (eV)	E_M (eV)	Vacancy formation energy (eV)
Dopant vacancy formation				
$CoFe_2O_4$	−390.0737	−381.6398	−13.5222	1.6728
$CuFe_2O_4$	−368.3630	−362.6943	−14.8575	1.9543
$ZnFe_2O_4$	−359.6753	−355.1706	−2.1075	3.4510
$MnFe_2O_4$	−410.5625	−400.4572	−35.5694	1.2130
Fe vacancy formation				
Fe_3O_4 (TV)	−299.8424	−289.5320	−15.3294	2.6457
Fe_3O_4 (OV)	−299.8424	−289.9661	−15.3294	2.2116
$CoFe_2O_4$	−390.0737	−378.8450	−15.3294	3.5640
$CuFe_2O_4$	−368.3630	−356.1419	−15.3294	4.5564
$ZnFe_2O_4$	−359.6753	−347.4861	−15.3294	4.5245
$MnFe_2O_4$	−410.5625	−400.4206	−15.3294	2.4772

released upon the addition of secondary metal ions. The ease of removal of an Fe atom (that corresponds to ease of leaching in experiments) was observed to be Fe_3O_4 (octahedral) > $MnFe_2O_4$ > Fe_3O_4 (tetrahedral) > $CoFe_2O_4$ > $ZnFe_2O_4$ > $CuFe_2O_4$ (Table 2). The same trend was observed experimentally (Fig. 4a–e), hinting towards a strong correlation between binding energies in the ferrite matrix and dissolution. Along similar lines, when vacancy formation energy was calculated for the doped atoms (Mn/Co/Zn/Cu), the trend observed was $ZnFe_2O_4$ > $CuFe_2O_4$ > $CoFe_2O_4$ > $MnFe_2O_4$ (Table 2). Here, a high vacancy formation energy implies that the release of the ion would be more energetically expensive, and subsequently less favourable. A similar trend was observed experimentally, with Cu and Zn release being the least and Mn release being the highest. DFT thus proves to be accurate for qualitatively predicting ion release rates from doped ferrites. It is to be noted that though we use ideal, bulk structures in our simulations, we are still able to predict the relative leaching rates of either Fe or a dopant atom by means of relatively inexpensive, but highly accurate vacancy formation energy calculations *via* DFT.

Variation in intracellular uptake of doped ferrite nanoparticles

Fig. S3† shows the intracellular uptake of all ferrite variants in A549 cells after 24 h, 48 h and 72 h of exposure using ICP-MS. Cellular uptake increased with exposure time across all the ferrite variants. The unit μg per cell was used to express the mass of nanoparticles uptake per individual cells. The cells were exposed to similar masses of individual ferrite nanoparticles, which were prepared as a stock solution in mass by volume method. The general trend in cellular uptake observed after 24 h of exposure is $Co_xFe_{3-x}O_4$ (3.46×10^{-5} μg per cell) > $Mn_xFe_{3-x}O_4$ (2.17×10^{-5} μg per cell) > $Cu_xFe_{3-x}O_4$ (1.84×10^{-5} μg per cell), Fe_3O_4 (1.82×10^{-5} μg per cell) > $Zn_xFe_{3-x}O_4$ (1.29×10^{-5} μg per cell). In contrast, the uptake was increased dramatically in the case of $Zn_xFe_{3-x}O_4$ after 48 h and 72 h. The cell uptake was calculated to be 68% (48 h) and 168% (72 h) with respect to the uptake values after 24 h. Similarly, the cell uptake of $Cu_xFe_{3-x}O_4$ was 40.7% and 84.18% at 48 h and 72 h, respectively with respect to the cell uptake values of $Cu_xFe_{3-x}O_4$ after 24 h. The trend of cell uptake magnitude after 48 h and 72 h exposure was $Zn_xFe_{3-x}O_4$ > $Cu_xFe_{3-x}O_4$ > $Co_xFe_{3-x}O_4$ > $Mn_xFe_{3-x}O_4$ > Fe_3O_4. Parallels can be drawn between the observations of the dissolution study and the corresponding uptake measurements. For example, $Cu_xFe_{3-x}O_4$ and $Zn_xFe_{3-x}O_4$ showed a similar % dissolution profile and cellular uptake profile.

$Co_xFe_{3-x}O_4$ having shown the highest amounts of dissolution up to 48 h, consequently, ends up having high cell uptake, while $Zn_xFe_{3-x}O_4$ having shown the lowest dissolution, ends up having low cell uptake, over the 48 h period. The correlation between dissolution and uptake however is not observed for the 72 h time point. The primary reason for this, especially in the case of $Mn_xFe_{3-x}O_4$ appears to be cell death (Fig. 5c), which results in cells getting eliminated during the washing step leading to lower cell density. Another reason for these trends could be a significant dissolution of the particulates into ions, as a consequence of which the cell uptake gets altered. Further, ionic uptake occurs through the diffusion process through ion channels, which is relatively a quicker and spontaneous process as compared to the particulate uptake in the cell. Therefore, it could be observed that the ferrites that generate sustained dissolved species correspond to higher intracellular uptake as compared to the ones that are least dissolving. It was observed through the TEM images (Fig. 2) and hydrodynamic stability studies (Fig. S4†) that there is a significant level of nanoparticles agglomeration present, particularly in the case of $Cu_xFe_{3-x}O_4$ and $Zn_xFe_{3-x}O_4$. However, the presence of smaller particles cannot be ruled out entirely from the systems, which consequently, enhances nanoparticle uptake in the cells. It was purely evident in the case of $Co_xFe_{3-x}O_4$ and $Mn_xFe_{3-x}O_4$ uptake, wherein higher suspension stability with smaller particle size enhanced overall percentage cell uptake. The correlation of cell uptake with toxicity and the role of ions compared to particulates has been discussed in subsequent sections.

Cytotoxicity of ferrites depends on their dissolution and uptake

A549 cells were treated with all the doped ferrite nanoparticle variants over a concentration range of 10–200 μg mL^{-1} for 24 h, 48 h and 72 h. Cell viability results indicated a dose-dependent behaviour (Fig. 5a–c) among all the ferrites, which is a conventional trend observed in most of the oxide nanoparticles.[5] For all tested ferrite nanoparticles, it was observed that with an increase in exposure concentration of the nanoparticles, there was a reduction in the cell viability. For 24 h of exposure studies, at lower concentration of 10 μg mL^{-1} most of the ferrite nanoparticles did not show significant reduction in cell

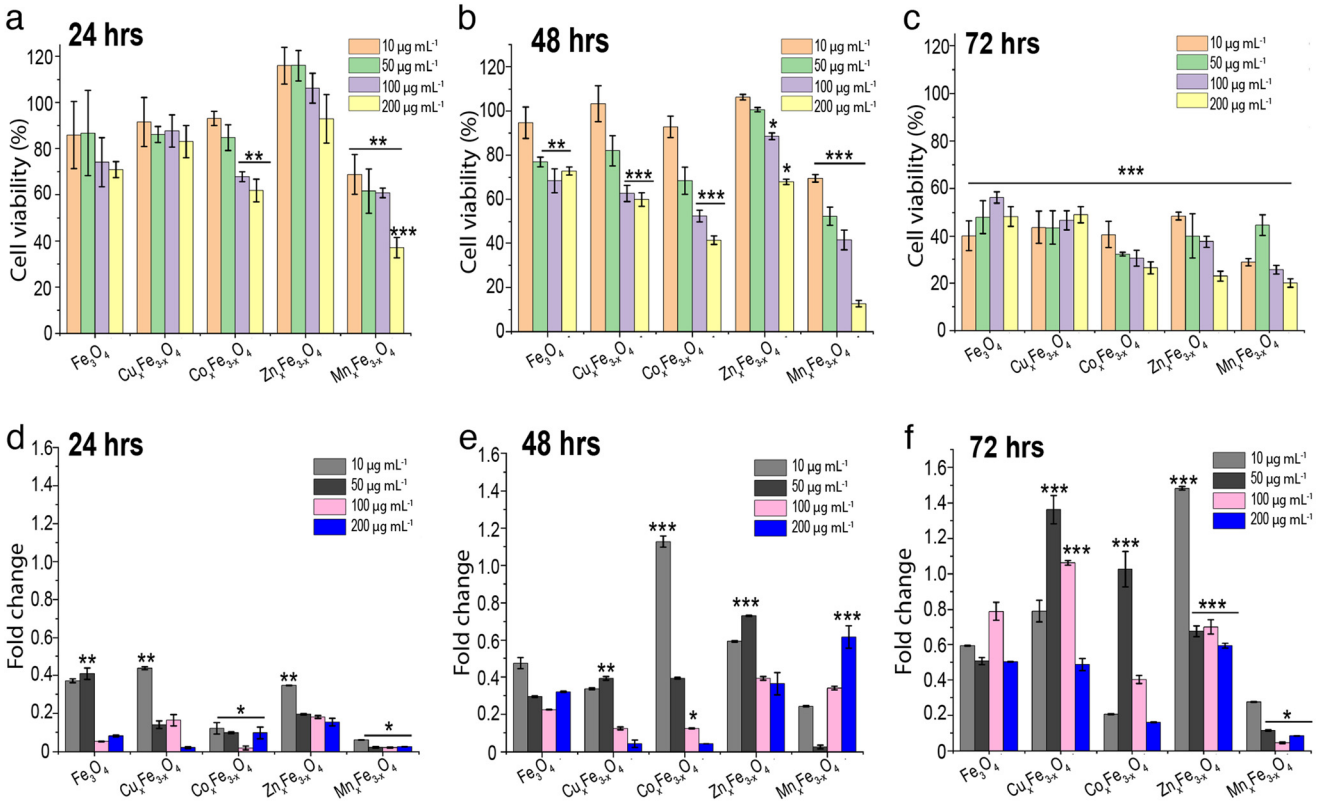

Fig. 5 Effect of doped ferrite nanoparticles on viability of A549 cells after (a) 24 h of exposure (b) 48 h of exposure (c) 72 h of exposure. Doped ferrite nanoparticle induced ROS generation after (d) 24 h of exposure (e) 48 h of exposure (f) 72 h of exposure, calculated as fold changes compared with control (n = 3, data presented as mean ± std.dev). The statistical analysis was performed with respect to control where *$p < 0.05$, **$p < 0.01$, and ***$p < 0.001$.

viability compared to control. However, $Mn_xFe_{3-x}O_4$ nanoparticles showed a significant reduction in cell viability across all the tested concentrations. By 48 h of exposure, a dose dependent cytotoxicity was observed across all the doped variants of ferrite nanoparticles. In comparison, the undoped Fe_3O_4 nanoparticles did not show a dose dependent response across all the three time points and showed lowest cytotoxicity among all the variants. When cells were exposed to 200 μg mL^{-1} of each variant of ferrite nanoparticles, there were significant reduction in cell viability (at each time point), particularly in the case of $Mn_xFe_{3-x}O_4$ and $Co_xFe_{3-x}O_4$. The reduction in cell viability at higher concentration might correspond to higher agglomeration and deposition of the particles on the cell surface leading to stresses on the cell surface.

As reported earlier, there is a trend showing higher nanoparticle dose enhances cell cytotoxicity. For ease of understanding and to make an argument, we are considering the exposure concentration of 100 μg mL^{-1} for further discussion. After 72 h, the reduction in cell viability was observed to be in the order of $Mn_xFe_{3-x}O_4$ > $Co_xFe_{3-x}O_4$ > $Zn_xFe_{3-x}O_4$ > $Cu_xFe_{3-x}O_4$ and Fe_3O_4. This observation exactly complements the argument of Fe_3O_4 being the least cytotoxic with respect to the other doped variants. $Mn_xFe_{3-x}O_4$ nanoparticles showed the least A549 cell viability, with more than a 75% reduction in cell viability after 72 h. Similarly, $Co_xFe_{3-x}O_4$ showed a similar trend, wherein, >70% cell death was observed after 72 h exposure. In the other variants *i.e.*, $Cu_xFe_{3-x}O_4$ and $Zn_xFe_{3-x}O_4$, the cell viability was reduced to 53% and 63% respectively after 72 h. Interestingly, $Zn_xFe_{3-x}O_4$, $Cu_xFe_{3-x}O_4$ and Fe_3O_4 nanoparticles showed a relatively less reduction in cell viability across all tested concentration ranges for up to 48 h of exposure. This interesting observation can be correlated with the low suspension stability and higher agglomeration (Fig. 4a), low % dissolution (Fig. 4f), and low uptake of nanoparticles (Fig. S3†). However, for $Co_xFe_{3-x}O_4$ and $Mn_xFe_{3-x}O_4$ nanoparticles, due to their suspension stability and high release of toxic elements Co and Mn, along with high intracellular uptake due to smaller size, significantly higher cell cytotoxicity was observed even at 24 h of exposure.

To investigate whether ROS generation plays a critical role in the cytotoxicity of the doped ferrite nanoparticle variants, the A549 cells were exposed to these particles in the presence of a ROS scavenger. All data for ROS fold changes are compared to the control. Results showed that after 24 h of exposure, all variants displayed between 0.02-fold to 0.43-fold ROS generation across a range of doses, with Fe_3O_4 (0.4-fold) and $Cu_xFe_{3-x}O_4$ (0.43-fold) showing slightly higher values at lower doses (Fig. 5d). After 48 h of exposure, $Co_xFe_{3-x}O_4$

(1.12-fold) showed high ROS values at low dose, while $Zn_xFe_{3-x}O_4$ (0.7-fold at 50 μg mL^{-1}) and $Mn_xFe_{3-x}O_4$ (0.6-fold at 200 μg mL^{-1}) showed high ROS values at higher doses (Fig. 5e). After 72 h of exposure, the ROS generation values varied over a wide range, with $Zn_xFe_{3-x}O_4$ (1.48-fold) and $Co_xFe_{3-x}O_4$ (1.2-fold) showing the highest values at 10 μg mL^{-1} and $Cu_xFe_{3-x}O_4$ (1.36-fold) showing high values at a larger exposed concentration (Fig. 5f). In most cases, $Mn_xFe_{3-x}O_4$ did not show high values of ROS generation because of a higher rate of cell death (Fig. 5a–c). Since ROS is generated by the living cells in response to stress, the presence of more dead cells in the wells wouldn't generate enough fluorescent signals to be detected by the spectrophotometer. For Fe_3O_4 nanoparticles, ROS production has been linked to the cytotoxic response.[33] The mechanism of damage involves Fe^{3+} reacting with H_2O_2 and $^{\bullet}O_2^-$ radicals produced by the mitochondria, leading to the formation of Fe^{2+} and hydroxyl radicals which tend to cause damage to the DNA and proteins.[34] In the case of $Zn_xFe_{3-x}O_4$, the production of oxidative stress is the most likely mechanism of toxicity. However, the toxicity is highly dependent on the medium in which the experiments are carried out. In the case of cell culture media, these nanoparticles tend to dissolve in the presence of amino acids and form complexes by binding to certain residues present in the media, making them potentially more toxic.[27,35,36]

The mechanism and factors causing the cytotoxicity of ferrites are highly complex, as observed in the data. In some cases, dissolution, size and stability of ferrites are playing a major factor ($Co_xFe_{3-x}O_4$ and $Mn_xFe_{3-x}O_4$) whereas in some cases, only dissolution of ionic species is playing a determining factor for causing toxicity. However, the suspension stability of ferrites nanoparticles is predominantly the major factor in governing dissolution, cellular uptake, bio-interaction, and cytotoxicity. For instance, $Cu_xFe_{3-x}O_4$ and $Zn_xFe_{3-x}O_4$ are the least hydrodynamically stable (Fig. S4a†), which causes the nanoparticles to deposit on the surface of the cell and cause cell membrane disruption.[37,38] The size of the nanoparticles has a significant impact on its cellular uptake. Smaller particle size and suspension stability can lead to better cell internalization and cause cytotoxicity through several processes. For instance, $Mn_xFe_{3-x}O_4$ nanoparticles have the smallest size (8.6 ± 2.7 nm; n = 100, $^{**}p < 0.01$) (Table 1) with higher suspension stability (Fig. S4a†) and therefore, has two ideal factors for enhanced cell uptake and particle-mediated toxicity. For $Cu_xFe_{3-x}O_4$ nanoparticles, the mechanism of damage includes the disruption of metal homeostasis, triggering of cell cycle progression, induction of metal alkalosis and ROS production.[3,39]

Furthermore, not just the dissolved species, the nanoparticle uptake through the endocytosis process followed by lysosomal-based intracellular dissolution also plays a major role in causing cytotoxicity. However, this process is relatively less rapid as compared to the extracellular dissolution of ferrites occurring in the cell culture medium. In the case of $Co_xFe_{3-x}O_4$, the surface charge at near-neutral pH is positive. Studies have shown that there is a preferential uptake of positively charged nanoparticles over neutral and negatively charged nanoparticles owing to favourable electrostatic interactions.[40,41] This increased uptake translates to higher cell toxicity through cell cycle arrest, cell apoptosis, and decreased metabolism.[42] Owing to the small size of $Co_xFe_{3-x}O_4$ nanoparticles and its ~8% dissolution, the uptake of these nanoparticles was higher in A549 cells leading to a reduction in cell viability along with increased ROS generation. Overall, there is a complex chain of events and factors responsible for causing cytotoxicity for these ferrite nanoparticles.

Cell uptake and cytotoxicity contributed by particulate and dissolved ions

In these sets of experiments, cell uptake and toxicity for each time point (24 h, 48 h and 72 h) were measured for two scenarios: a) an ionic control wherein 100% of the ferrite nanoparticles introduced to the media dissolved into ions, and b) an ionic control from the experimental dissolution data obtained from our experiments (Fig. S4†). In all cases, it was observed that the cell uptake was higher in the ionic control representing 100% dissolution as compared to the experimentally observed dissolution (Fig. 6a–e). The process of uptake wasn't time-dependent in the case of a complete dissolution scenario contrary to the actual dissolution scenario. In each variant of ferrites, the uptake of Fe ions and dopants (Zn, Mn, Cu, Co) increased with an increase in the incubation time. Several factors affect ionic uptake by the cells. Some of them include ionic concentration, organic and inorganic complexation of ions in the media, permeability of the ions and their complexes in the cells, ion saturation in the cells, active and passive ion transportation processes. The cells also control ionic homeostasis, wherein a fixed number of ions are permitted inside the cells for metabolic activities through the semipermeable membrane. However, if there is a loss of cell membrane integrity due to stress, there is a high chance that the ions diffuse inside the cells. Also, if we compare the cell uptake values of ferrites (Fig. S3†) with that of ionic uptake values in the actual dissolution scenario (Fig. 6a–e), the magnitude of intracellular uptake is lower in the latter case. It means that the magnitude of the cellular uptake has a contribution from both ionic and particulate uptake by the cells (Fig. 7a–e). Subsequently, cell viability was lower in ionic control representing 100% dissolution as compared to the experimentally observed dissolution (Fig. 6f–j). Exposure of ionic Fe representing complete dissolution from Fe_3O_4 nanoparticles reduced the cell viability to ~60% at the end of 72 h. In comparison, with an exposure of 3.61 μg mL^{-1} (representing the experimental Fe release concentration at 72 h), the cell viability was found to be >80% at the end of 72 h (Fig. S4a†). A similar trend is observed for all of the samples, wherein an ionic exposure

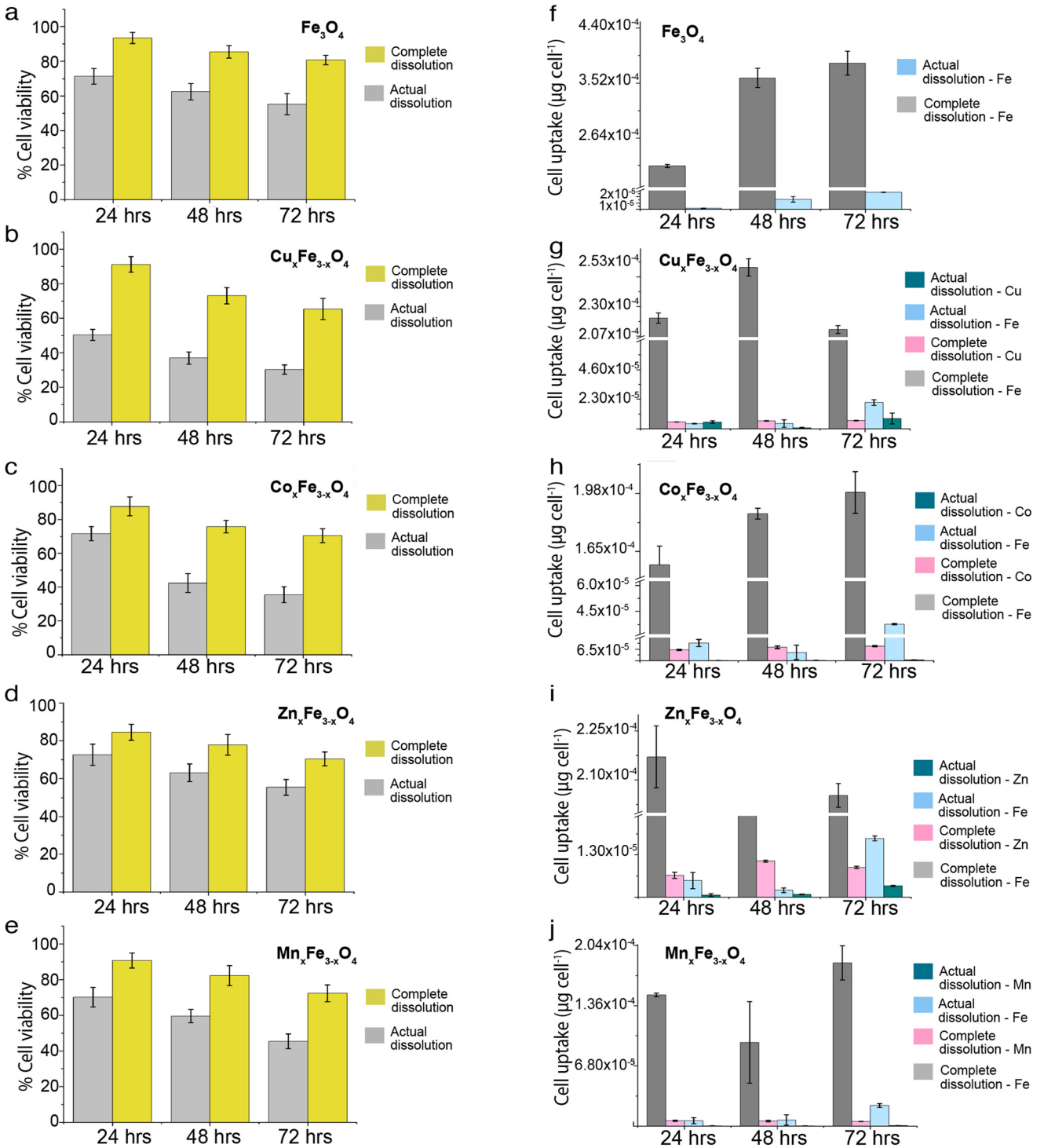

Fig. 6 Comparison of cell viability in the event of complete dissolution *versus* realistic dissolution for (a) Fe_3O_4 (b) $Cu_xFe_{3-x}O_4$ (c) $Co_xFe_{3-x}O_4$ (d) $Zn_xFe_{3-x}O_4$ (e) $Mn_xFe_{3-x}O_4$. Comparison of cell uptake of complete dissolution *versus* realistic dissolution for (f) Fe_3O_4 (g) $Cu_xFe_{3-x}O_4$ (h) $Co_xFe_{3-x}O_4$ (i) $Zn_xFe_{3-x}O_4$ (j) $Mn_xFe_{3-x}O_4$ (n = 3, data presented as mean ± std.dev, uptake was calculated with respect to untreated control). The exposure concentrations for complete and actual dissolution is shown in ESI† (Table S1).

representing 100% dissolution of the ferrite nanoparticles adversely affects the cell viability. In comparison, the cell viability remains >70% for all of the variants when exposed to the ionic counterparts representing the experimentally observed dissolution data. This certainly means that not just dissolved ions but nanoparticles have a significant role to play in enhancing the uptake and cytotoxicity of these ferrite nanoparticles.

Fig. 7 shows the contribution of ions and nanoparticles towards the toxicity of all the variants and supports clarifying

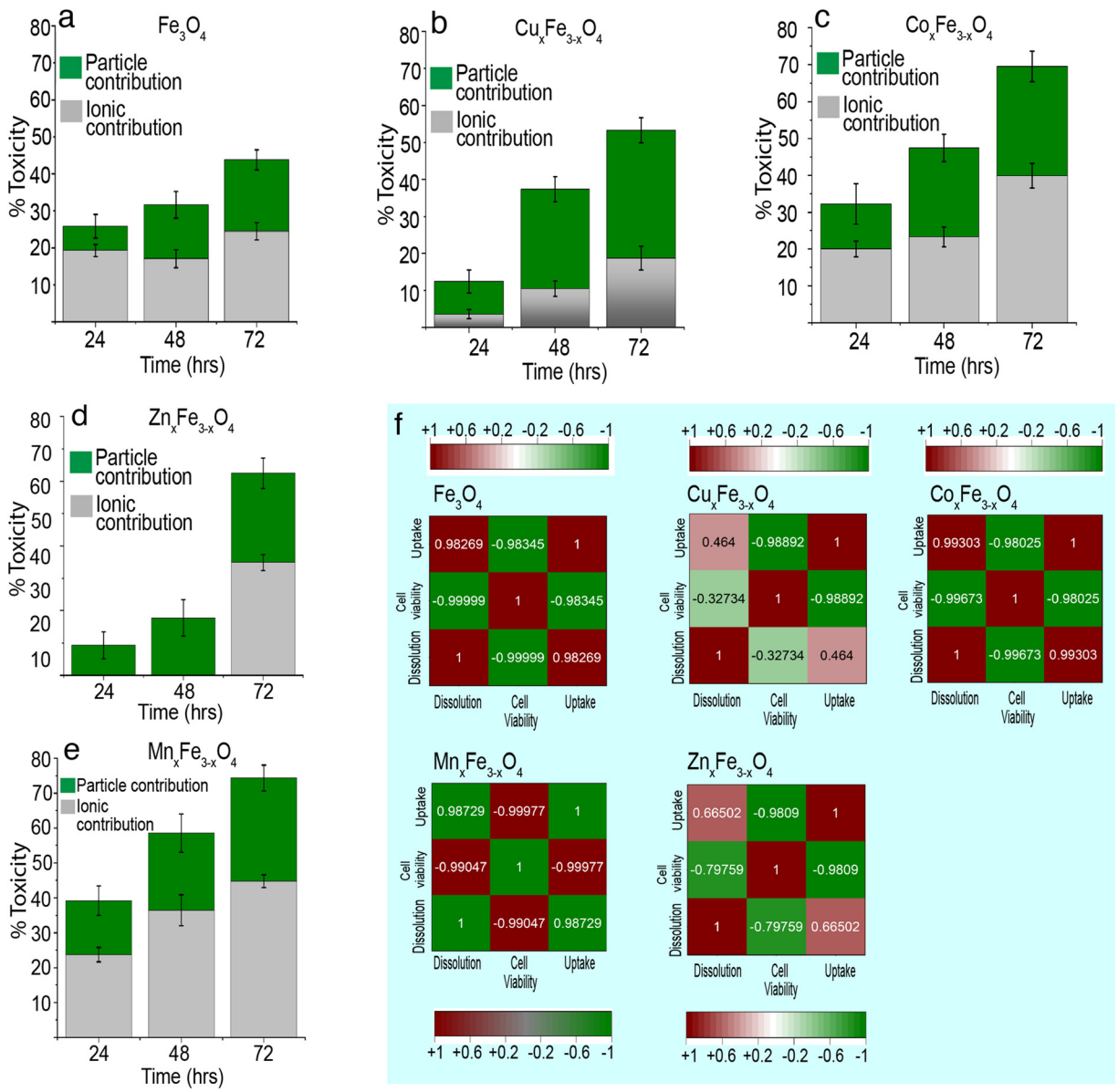

Fig. 7 Contribution of particulates and dissolved ions to the toxicity of for (a) Fe_3O_4 (b) $Cu_xFe_{3-x}O_4$ (c) $Co_xFe_{3-x}O_4$ (d) $Zn_xFe_{3-x}O_4$ (e) $Mn_xFe_{3-x}O_4$. The experiments were performed in triplicate (n = 3) and the uptake were calculated with respected to untreated control, considered exposure concentration is 100 μg mL^{-1} (f) correlation plots for dissolution, cell viability and uptake for Fe_3O_4, $Cu_xFe_{3-x}O_4$, $Co_xFe_{3-x}O_4$, $Zn_xFe_{3-x}O_4$, $Mn_xFe_{3-x}O_4$. The plots were prepared using the Pearson's correlation coefficient and were plotted using the origin lab software.

the hypothesis stated above. While in the case of $Cu_xFe_{3-x}O_4$ and $Zn_xFe_{3-x}O_4$, most of the toxicity is due to the dissolved ions, the same cannot be said about the other two variants. Possible reasons for such an observation could be the formation of large agglomerates of $Cu_xFe_{3-x}O_4$ and $Zn_xFe_{3-x}O_4$ nanoparticles which reduces the contribution from nanoparticulate form and inherent toxicity of Cu and Zn ions. Even though the toxicity of $Cu_xFe_{3-x}O_4$ and $Zn_xFe_{3-x}O_4$ wasn't significantly higher up to 48 h of exposure, the dissolution profile of $Cu_xFe_{3-x}O_4$ (Fig. 4b) and $Zn_xFe_{3-x}O_4$ (Fig. 4d) showed a release of 0.88 ± 0.01 and 0.4 ± 0.01 μg mL^{-1} of Cu and Zn ions respectively after 48 h, that played a role in causing initial toxicity. In the case of $Co_xFe_{3-x}O_4$ and $Mn_xFe_{3-x}O_4$, both particulates and dissolved species play a role in the toxicological impact on the cells. This could be well correlated with the hydrodynamic stability of both these particles (Fig. S4a†) and the dissolution data (Fig. 5c and e). Better suspension stability would help the particulate contribution towards toxicity and enhance the dissolution process. Therefore, both factors are contributing to cellular toxicological impact. Put together, it can be inferred that the toxicity of $Co_xFe_{3-x}O_4$ and $Mn_xFe_{3-x}O_4$ is contributed to by both particulates and ions, whereas for $Cu_xFe_{3-x}O_4$ and $Zn_xFe_{3-x}O_4$ toxicity is largely due to the dissolved ions as opposed to particulates. Based on dissolution data (Fig. 4a–e), we performed a cytotoxicity analysis using ionic control of

respective dopant ions at an equivalent concentration of dissolved species generated at various time points (24 h, 48 h, 72 h). It was observed that, there is a contribution from the dopant ions in causing toxicity (Table S3†).

Correlation between dissolution, uptake and cell viability

There isn't a linear correlation between dissolution, cell viability and cell uptake for all variants (Fig. 7). For example, in the case of $Cu_xFe_{3-x}O_4$, there is a weak positive correlation between dissolution and cell uptake (0.46) and a weak negative correlation between dissolution and cell viability (−0.32). This implies that in spite of dissolution, there isn't a large amount of cellular uptake of the nanoparticle or the dissolved ion and consequently, the toxicity isn't as high either. Something similar can also be observed for $Zn_xFe_{3-x}O_4$ nanoparticles, with a weak positive correlation between dissolution and cell uptake (0.66) and a moderate negative correlation between dissolution and cell viability (−0.79). Therefore, it can be concluded that the toxicological impact of ferrites is not straightforward. It is this inconsistency in trends across all experiments carried out in this study that makes safety-by-design not only challenging but also critical to ensure considerations to safety have been thoroughly addressed before these nanomaterials are used on industrial scales. Fe_3O_4 has a lower tendency to dissolve. Due to this, Fe_3O_4 shows less toxicity, and majority of the toxicity comes from their particulate. However, the introduction of transition metal dopants is increasing the tendency of ferrites to dissolve. This could be because of structural changes, changes to hydrodynamic stability or the overall chemical stability of the material. Due to this reduced stability, there is a release of toxic metal ions into the media. Here, it is important to note that the amount of surface area exposed to the medium also plays a crucial role in the formation of complexes and the rate of dissolution.

Relative change in toxicity of metal-oxide nanoparticles on doping

The observations of this study give rise to an interesting discussion on the impact of doping of metal-oxide nanoparticles on its reactivity and toxicity. Although it is acknowledged that the properties of nanoparticles can be altered through doping, considerations of safety upon long-term exposure to biological and environmental entities are essential to ascertain their fitness for large-scale usage. A mini-review was conducted to observe the relative change in the toxicity of commonly used metal-oxide nanoparticles (CuO, ZnO, TiO_2 and CeO_2) upon doping (Fig. 8). Of particular interest is the number of doped variants above and below the baseline toxicity for each nanoparticle set. While in some cases doping of CuO nanoparticles led to an increase in toxicity (*e.g.* Ag doping[43]), largely, there was a decrease in toxicity after doping (Fig. 8a). In particular, on doping with Sn or Fe,[3,44] the largest relative shift below the baseline toxicity was observed. The data indicate that doping may serve to be a viable strategy for improving the safety of CuO for large-scale applications.

In the case of ZnO nanoparticles (Fig. 8b), doping was seen to have both positive and negative impacts on relative toxicity. While dopants such as Mg, Ag, and La showed the best positive impact on toxicity (largest shifts below the baseline), 5% La showed the worst negative impact (largest shifts above the baseline).[45,46] The data suggests that similar to CuO nanoparticles, doping can drastically

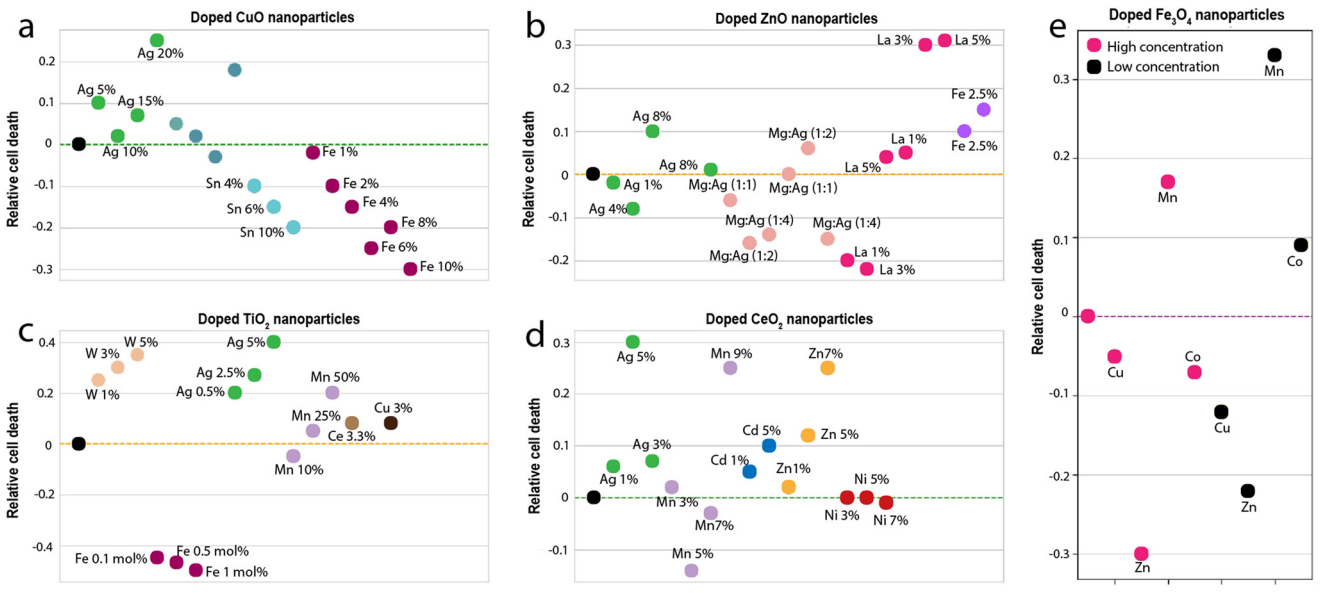

Fig. 8 Comparison of the relative toxicity (a) doped CuO nanoparticles (b) doped ZnO nanoparticles (c) doped TiO_2 nanoparticles (d) doped CeO_2 nanoparticles and (e) doped ferrite nanoparticles. The dotted line in each case is the baseline (the toxicity of the undoped nanoparticle). The data and references used to generate these graphs is reported in the ESI.†

improve the toxicity of ZnO nanoparticles. TiO_2 nanoparticles, on the other hand, are considerably safe, as is evidenced by their widespread usage for biomedical applications.[47,48] Therefore, it comes as no surprise that in most cases, upon doping, the toxicity of TiO_2 nanoparticles increases (Fig. 8c). Only in rare cases (such as doping with particular concentrations of Fe)[49] was a reduction in toxicity observed. The data thus suggests that doping may not be a viable strategy for improving the safety of TiO_2 nanoparticles. CeO_2 nanoparticles show similar behaviour to TiO_2 nanoparticles (Fig. 8d). In all cases except for Mn doping, the toxicity of CeO_2 increased on doping.

In comparison to these metal-oxide nanoparticles, ferrites are rather neutral. The behaviour of ferrite nanoparticles in this respect, closely resembles that of ZnO nanoparticles. On doping, there is either a drastic increase or decrease in toxicity. For *e.g.*, doping with Zn significantly decrease the toxicity (largest shift below the baseline), while doping with Mn, results in a significant increase (largest shift above the baseline). However, these inferences aren't straightforward because the toxicological impact has a direct correlation with their suspension stability and dissolution of nanoparticles.

Conclusions

In this study, by combining experimental and computational approaches, we have quantitatively identified trends in the dissolution of ferrite nanoparticles and their correlation to toxicity. We synthesized variants of ferrite nanoparticles doped with transition metal ions (Cu, Zn, Mn and Co) and characterized them using a range of physicochemical techniques (TEM, XRD, XPS, ICP-MS). Suspension characteristics of these nanoparticles for up to 72 h was measured to quantitatively identify the release of Fe and dopant ions from the nanoparticles. We found that on doping with transition metal ions, there was a decrease in the release of Fe ions from the ferrite matrix, an observation that was backed up by vacancy formation energy calculations performed using DFT. $Co_xFe_{3-x}O_4$ nanoparticles, showed ~8% dissolution, had a higher uptake leading to a reduction in cell viability along with increased ROS. Toxicity of $Co_xFe_{3-x}O_4$ and $Mn_xFe_{3-x}O_4$ is contributed both by the particulates and ions, whereas for $Cu_xFe_{3-x}O_4$ and $Zn_xFe_{3-x}O_4$ toxicity is largely due to the dissolved ions as opposed to particulates. The correlation analysis between cell viability, cell uptake, dissolution and toxicity highlighted that the overall reasons for causing toxicological impact after the introduction of dopant in ferrites aren't straightforward. While ferrite nanoparticles are safer than their metal-oxide nanoparticle counterparts (CuO, ZnO), the introduction of transition metal elements as dopants into the ferrite matrix for enhancing properties can thus impact the safety of ferrites. This study tried to correlate the various properties of doped ferrite nanoparticles and investigate their impact on safety-by-design and toxicology.

Author contributions

SC: experimentation, conceptualization, editing; DM: data analysis, computational studies, editing; VSAV: synthesis of ferrites; MS and RR: computational studies and editing; PZ and SM: data analysis, conceptualization, editing.

Conflicts of interest

The authors declare that they have no known competing financial interests or personal relationships that could have appeared to influence the work reported in this study.

Acknowledgements

The authors acknowledge the funds received from SERB-CRG project (CRG/2019/006165; FIST funded microscopy), SC acknowledges NERC-Discovery Sciences-Discipline Hopping project (Grant number: NE/X017559/1).

References

1 Z. Ma, J. Mohapatra, K. Wei, J. P. Liu and S. Sun, Magnetic nanoparticles: Synthesis, anisotropy, and applications, *Chem. Rev.*, 2021, **123**, 3904–3943.
2 H. Gavilán, S. K. Avugadda, T. Fernández-Cabada, N. Soni, M. Cassani, B. T. Mai, R. Chantrell and T. Pellegrino, Magnetic nanoparticles and clusters for magnetic hyperthermia: Optimizing their heat performance and developing combinatorial therapies to tackle cancer, *Chem. Soc. Rev.*, 2021, **50**, 11614–11667.
3 H. Naatz, S. Lin, R. Li, W. Jiang, Z. Ji, C. H. Chang, J. Köser, J. Thöming, T. Xia, A. E. Nel and L. Mädler, Safe-by-design CuO nanoparticles via Fe-doping, Cu–O bond length variation, and biological assessment in cells and zebrafish embryos, *ACS Nano*, 2017, **11**, 501–515.
4 B. Nowack and T. D. Bucheli, Occurrence, behavior and effects of nanoparticles in the environment, *Environ. Pollut.*, 2007, **150**, 5–22.
5 S. Sharifi, S. Behzadi, S. Laurent, M. L. Forrest, P. Stroeve and M. Mahmoudi, Toxicity of nanomaterials, *Chem. Soc. Rev.*, 2012, **41**, 2323–2343.
6 P. P. Fu, Q. Xia, H. M. Hwang, P. C. Ray and H. Yu, Mechanisms of nanotoxicity: generation of reactive oxygen species, *J. Food Drug Anal.*, 2014, **22**, 64–75.
7 P. C. Ray, H. Yu and P. P. Fu, Toxicity and environmental risks of nanomaterials: challenges and future needs, *J. Environ. Sci. Health, Part C: Environ. Carcinog. Ecotoxicol. Rev.*, 2009, **27**, 1–35.
8 A. Nel, T. Xia, L. Madler and N. Li, Toxic potential of materials at the nanolevel, *Science*, 2006, **311**, 622–627.
9 M. N. Moore, Do nanoparticles present ecotoxicological risks for the health of the aquatic environment?, *Environ. Pollut.*, 2006, **32**, 967–976.

10 C. Guo, R. J. Weber, A. Buckley, J. Mazzolini, S. Robertson, J. M. Delgado-Saborit, J. Z. Rappoport, J. Warren, A. Hodgson, P. Sanderson and J. K. Chipman, Environmentally relevant iron oxide nanoparticles produce limited acute pulmonary effects in rats at realistic exposure levels, *Int. J. Mol. Sci.*, 2021, **22**, 556.

11 G. Liu, J. Gao, H. Ai and X. Chen, Applications and potential toxicity of magnetic iron oxide nanoparticles, *Small*, 2013, **9**, 1533–1545.

12 S. J. Soenen, N. Nuytten, S. F. De Meyer, S. C. De Smedt and M. De Cuyper, High intracellular iron oxide nanoparticle concentrations affect cellular cytoskeleton and focal adhesion kinase-mediated signaling, *Small*, 2010, **6**, 832–842.

13 J. T. Kwon, S. K. Hwang, H. Jin, D. S. Kim, A. Minai-Tehrani, H. J. Yoon, M. Choi, T. J. Yoon, D. Y. Han, Y. W. Kang and B. I. Yoon, Body distribution of inhaled fluorescent magnetic nanoparticles in the mice, *J. Occup. Health*, 2008, **50**, 1–6.

14 M. Bohra, V. Alman and R. Arras, Nanostructured $ZnFe_2O_4$: an exotic energy material, *Nanomaterials*, 2021, **11**, 1286.

15 S. Tao, F. Gao, X. Liu and O. T. Sørensen, Preparation and gas-sensing properties of CuFe2O4 at reduced temperature, *Mater. Sci. Eng., B*, 2000, **77**, 172–176.

16 J. S. Sagu, K. G. Wijayantha and A. A. Tahir, The pseudocapacitive nature of CoFe2O4 thin films, *Electrochim. Acta*, 2017, **246**, 870–878.

17 T. Ahn, J. H. Kim, H. M. Yang, J. W. Lee and J. D. Kim, Formation pathways of magnetite nanoparticles by coprecipitation method, *J. Phys. Chem. C*, 2012, **116**, 6069–6076.

18 A. B. Djurišić, Y. H. Leung, A. M. Ng, X. Y. Xu, P. K. Lee, N. Degger and R. S. Wu, Toxicity of metal oxide nanoparticles: mechanisms, characterization, and avoiding experimental artefacts, *Small*, 2015, **11**, 26–44.

19 J. Hafner, Ab-initio simulations of materials using VASP: Density-functional theory and beyond, *J. Comput. Chem.*, 2008, **29**, 2044–2078.

20 J. Enkovaara, C. Rostgaard, J. J. Mortensen, J. Chen, M. Dułak, L. Ferrighi, J. Gavnholt, C. Glinsvad, V. Haikola, H. A. Hansen and H. H. Kristoffersen, Electronic structure calculations with GPAW: a real-space implementation of the projector augmented-wave method, *J. Phys.: Condens. Matter*, 2010, **22**, 253202.

21 P. Giannozzi, S. Baroni, N. Bonini, M. Calandra, R. Car, C. Cavazzoni, D. Ceresoli, G. L. Chiarotti, M. Cococcioni, I. Dabo and A. Dal Corso, QUANTUM ESPRESSO: a modular and open-source software project for quantum simulations of materials, *J. Phys.: Condens. Matter*, 2009, **21**, 395502.

22 J. P. Perdew, K. Burke and M. Ernzerhof, Generalized gradient approximation made simple, *Phys. Rev. Lett.*, 1996, **77**, 3865.

23 C. Freysoldt, B. Grabowski, T. Hickel, J. Neugebauer, G. Kresse, A. Janotti and C. G. Van de Walle, First-principles calculations for point defects in solids, *Rev. Mod. Phys.*, 2014, **86**, 253.

24 C. G. Van de Walle and J. Neugebauer, First-principles calculations for defects and impurities: Applications to III-nitrides, *J. Appl. Phys.*, 2004, **95**, 3851–3879.

25 T. Wang, W. Yang, T. Song, C. Li, L. Zhang, H. Wang and L. Chai, Cu doped Fe_3O_4 magnetic adsorbent for arsenic: synthesis, property, and sorption application, *RSC Adv.*, 2015, **5**, 50011–50018.

26 F. Y. Cheng, C. H. Su, Y. S. Yang, C. S. Yeh, C. Y. Tsai, C. L. Wu, M. T. Wu and D. B. Shieh, Characterization of aqueous dispersions of Fe_3O_4 nanoparticles and their biomedical applications, *Biomaterials*, 2005, **26**, 729–738.

27 D. T. Harvey and R. W. Linton, Chemical characterization of hydrous ferric oxides by X-ray photoelectron spectroscopy, *Anal. Chem.*, 1981, **53**, 1684–1688.

28 Y. Meng, D. Chen and X. Jiao, Synthesis and characterization of $CoFe_2O_4$ hollow spheres, *Eur. J. Inorg. Chem.*, 2008, **25**, 4019–4023.

29 S. Chinnapaiyan, T. W. Chen, S. M. Chen, Z. A. Alothman, M. A. Ali, S. M. Wabaidur, F. Al-Hemaid, S. Y. Lee and W. H. Chang, Ultrasonic-assisted preparation and characterization of magnetic $ZnFe_2O_4$/g-C3N4 nanomaterial and their applications towards electrocatalytic reduction of 4-nitrophenol, *Ultrason. Sonochem.*, 2020, **68**, 105071.

30 S. L. Pinho, G. A. Pereira, P. Voisin, J. Kassem, V. Bouchaud, L. Etienne, J. A. Peters, L. Carlos, S. Mornet, C. F. Geraldes and J. Rocha, Fine tuning of the relaxometry of γ-Fe_2O_3@SiO_2 nanoparticles by tweaking the silica coating thickness, *ACS Nano*, 2010, **4**(9), 5339–5349.

31 S. Wang, J. Tang, H. Zhao, J. Wan and K. Chen, Synthesis of magnetite–silica core–shell nanoparticles via direct silicon oxidation, *J. Colloid Interface Sci.*, 2014, **432**, 43–46.

32 S. K. Misra, A. Dybowska, D. Berhanu, S. N. Luoma and E. Valsami-Jones, The complexity of nanoparticle dissolution and its importance in nanotoxicological studies, *Sci. Total Environ.*, 2012, **438**, 225–232.

33 R. J. Wydra, P. G. Rychahou, B. M. Evers, K. W. Anderson, T. D. Dziubla and J. Z. Hilt, The role of ROS generation from magnetic nanoparticles in an alternating magnetic field on cytotoxicity, *Acta Biomater.*, 2015, **25**, 284–290.

34 M. Watanabe, M. Yoneda, A. Morohashi, Y. Hori, D. Okamoto, A. Sato, D. Kurioka, T. Nittami, Y. Hirokawa, T. Shiraishi and K. Kawai, Effects of Fe3O4 magnetic nanoparticles on A549 cells, *Int. J. Mol. Sci.*, 2013, **14**, 15546–15560.

35 M. N. Martin, A. J. Allen, R. I. MacCuspie and V. A. Hackley, Dissolution, agglomerate morphology, and stability limits of protein-coated silver nanoparticles, *Langmuir*, 2014, **30**, 11442–11452.

36 S. Chakraborty, A. Nair, M. Paliwal, A. Dybowska and S. K. Misra, Exposure media a critical factor for controlling dissolution of CuO nanoparticles, *J. Nanopart. Res.*, 2018, **20**, 1–4.

37 K. L. Chen and G. D. Bothun, Nanoparticles meet cell membranes: probing nonspecific interactions using model membranes, *Environ. Sci. Technol.*, 2014, **48**, 873–880.

38 A. Lesniak, A. Salvati, M. J. Santos-Martinez, M. W. Radomski, K. A. Dawson and C. Åberg, Nanoparticle adhesion to the cell membrane and its effect on nanoparticle uptake efficiency, *J. Am. Chem. Soc.*, 2013, **135**(4), 1438–1444.

39 E. Moschini, M. Gualtieri, M. Colombo, U. Fascio, M. Camatini and P. Mantecca, The modality of cell–particle interactions drives the toxicity of nanosized CuO and TiO_2 in human alveolar epithelial cells, *Toxicol. Lett.*, 2013, **222**, 102–116.

40 A. Verma and F. Stellacci, Effect of surface properties on nanoparticle–cell interactions, *Small*, 2010, **6**, 12–21.

41 V. Forest, M. Cottier and J. Pourchez, Electrostatic interactions favor the binding of positive nanoparticles on cells: A reductive theory, *Nano Today*, 2015, **10**, 677–680.

42 F. Ahmad, X. Liu, Y. Zhou and H. Yao, An in vivo evaluation of acute toxicity of cobalt ferrite (CoFe2O4) nanoparticles in larval-embryo Zebrafish (Danio rerio), *Aquat. Toxicol.*, 2015, **166**, 21–28.

43 D. R. Preethi, S. Prabhu, V. Ravikumar and A. Philominal, Anticancer activity of pure and silver doped copper oxide nanoparticles against A549 Cell line, *Mater. Today Commun.*, 2022, **33**, 104462.

44 T. Jan, J. Iqbal, U. Farooq, A. Gul, R. Abbasi, I. Ahmad and M. Malik, Structural, Raman and optical characteristics of Sn doped CuO nanostructures: a novel anticancer agent, *Ceram. Int.*, 2015, **41**, 13074–13079.

45 K. Hamidian, M. Sarani, M. Barani and F. Khakbaz, Cytotoxic performance of green synthesized Ag and Mg dual doped ZnO NPs using Salvadora persica extract against MDA-MB-231 and MCF-10 cells, *Arabian J. Chem.*, 2022, **15**, 103792.

46 M. Shakir, M. Faraz, M. A. Sherwani and S. I. Al-Resayes, Photocatalytic degradation of the Paracetamol drug using Lanthanum doped ZnO nanoparticles and their in-vitro cytotoxicity assay, *J. Lumin.*, 2016, **176**, 159–167.

47 Z. F. Yin, L. Wu, H. G. Yang and Y. H. Su, Recent progress in biomedical applications of titanium dioxide, *Phys. Chem. Chem. Phys.*, 2013, **15**, 4844–4858.

48 S. Wu, Z. Weng, X. Liu, K. W. Yeung and P. K. Chu, Functionalized TiO_2 based nanomaterials for biomedical applications, *Adv. Funct. Mater.*, 2014, **24**, 5464–5481.

49 T. Barkhade, S. Mishra, H. Chander, S. K. Mahapatra and I. Banerjee, Effect of TiO_2 and Fe doped TiO_2 nanoparticles on mitochondrial membrane potential in HBL-100 cells, *Biointerphases*, 2019, **14**, 041003.